Nanomolding of Topological Materials for Interconnects

CNF Summer Student: Richard A. Remias
Student Affiliation: Physics, University of Rhode Island

Summer Program(s): 2024 Cornell NanoScale Facility Research Experience for Undergraduates (CNF REU) Program

Principal Investigator(s): Judy Cha, Materials Science and Engineering, Cornell University

Mentor(s): Quynh Sam, Khoan Duong; Materials Science and Engineering, Cornell University

Primary Source(s) of Research Funding: National Science Foundation under Grant No. NNCI-2025233

Contact: riskoalbi@live.com, jc476@cornell.edu, qps2@cornell.edu, nd399@cornell.edu

Summer Program Website: https://cnf.cornell.edu/education/reu/2024

Primary CNF Tools Used: Oxford FlexAl ALD, Zeiss Supra SEM, Bruker EDX, Veeco Icon AFM, Woollam RC2 Ellipsometer

Abstract:

The increasing resistivity of copper (Cu) interconnects with decreasing dimensions poses many challenges for the continued downscaling of integrated circuits and computer chips. At the nanoscale, electron scattering at grain boundaries and surfaces of the interconnects causes an increase in resistivity leading to higher energy consumption and signal delay in computer chips. Conversely, topological materials may show decreasing resistivity with decreasing size at nanoscale dimensions due to their topologically protected band structures that are predicted to suppress electron scattering. Thus, transport studies of topological materials at the nanoscale are critical to find alternative metals to Cu interconnects. Nevertheless, current nanowire synthesis methods such as molecular beam epitaxy (MBE) and chemical vapor transport (CVT) struggle to create uniformly sized nanowires.

We use nanomolding to fabricate nanowires of topological materials, where a bulk material is pressed into a porous anodic aluminum oxide (AAO) mold to create high aspect ratio nanowires. To promote more facile nanomolding and to prevent oxidation of the molded nanowires, we coat the AAO mold pore walls with a thin film of aluminum nitride (AlN) and tantalum nitride (TaN). The CNF's Oxford FlexAl atomic layer deposition (ALD) tool is used to deposit precise and uniform films due to its self-limiting reactions. Through energy dispersive X-ray spectroscopy (EDX), we determine the infiltration depth of AlN in our pores. Additionally, InBi is a topological material which may exhibit interesting quantum properties at few-layer thicknesses.

We use nanomolding to compress InBi into thin flakes by encapsulating the InBi with hexagonal boron nitride (hBN). The CNF's AFM Veeco Icon tool is used to determine the resulting thickness of the InBi flake.

Summary of Research:

ALD was first used to deposit 20 nm of AlN onto the AAO mold which had a pore diameter of 120 nm. This deposition was done at 400°C for 334 cycles at 0.6 Å/cycle, using trimethylaluminum (TMA) and H2/N2 plasma as precursors. These precursors were pulsed for 0.02 seconds and 5 seconds, respectively. To estimate deposition thickness, a blank silicon substrate was placed next to the mold in the ALD chamber and ellipsometry was used to determine the thickness of AlN deposited onto the substrate. The resulting thickness was estimated to be about 18.02 ± 0.027 nm. A scanning electron microscope (SEM) was then used to take a cross-sectional image of the AAO mold which was combined with EDX to map the elements deposited within the mold channel walls. However, due to low film thickness and low atomic weight of nitrogen, the infiltration depth of AlN in our pores was inconclusive as no nitrogen was detected on the pore walls (Figure 1).

Next, we used ALD to deposit 10 nm of TaN onto a mold of identical pore diameter. This deposition was done at 250°C for 250 cycles at 0.4 Å/cycle, using tris(diethylamido)(tert-butylimido)tantalum(V), or TBTDET, and ammonia (NH3) as precursors. The pulse time for these precursors was 6 seconds and 15 seconds, respectively. The same method was used to estimate the deposited film thickness, which was determined to be 6.87 ± 0.081 nm. SEM was used to take a cross-sectional image and EDX was used for element mapping. Unfortunately, no tantalum was detected in the pores so the infiltration depth of TaN is inconclusive (Figure 2). Through improvements in ALD parameters, we may be able to determine infiltration depth using EDX.

Additionally, we used nanomolding to press InBi into thin flakes. This was done by placing an hBN flake both on top of and underneath the InBi piece to create an hBN-InBi-hBN stack. The stack was made using tape

exfoliation and the desired flakes of uniform thickness were found under a microscope and transferred using a glass slide with an epoxy drop. We used a hot press to compress the InBi stack at 80°C for 15 minutes. The resulting stack is shown in Figure 3.

To determine the final thickness, we used atomic force microscopy to create a line profile over the stack. We measured the thickness of InBi to be 35.9 nm (Figure 4). Different nanomolding parameters were also used on different stacks, such as pressing for 30 minutes at 100°C, however, no flakes were pressed to be thinner than 35.9 nm.

Conclusions and Future Steps:

EDX results after deposition of AlN and TaN show that a more sensitive elemental mapping method may be needed for accurate determination of infiltration depth into AAO channel pores. A method such as X-ray photoelectron spectroscopy may be more sensitive to thinner films as well as lighter elements. Also, increasing precursor pulse time in ALD processes may allow more time for gases to travel into high aspect ratio features, increasing infiltration depth. Increasing gas flow rates may also prove useful as it will increase delivery of gases deeper into the pores.

Results also show that nanomolding can be used to create sub 40 nm thin InBi flakes. Future work would include removing the top hBN flake and testing the resistance of the InBi flake.

Acknowledgements:

This work was made possible by the Cornell NanoScale Facility and funded by the National Science Foundation via grant no. NNCI-2025233. Special thanks to Judy Cha, Quynh Sam, Khoan Duong, Sihun Lee, and Melanie-Claire Mallison for their great help and guidance.

References:

[1] Chen, L., Wu, A.X., Tulu, N., et al. Exceptional electronic transport and quantum oscillations in thin bismuth crystals grown inside van der Waals materials. Nat. Mater. 23, 741–746 (2024). https://doi.org/10.1038/s41563-024-01894-0.

[2] Kiani, M. T., Sam, Q. P., Jin, G., Pamuk, B., Han, H. J., Hart, J. L., Stauff, J., and Cha, J. J. (2023). Nanomolding of metastable Mo4P3. Matter, 6(6), 1894–1902. https://doi.org/10.1016/j.matt.2023.03.023.

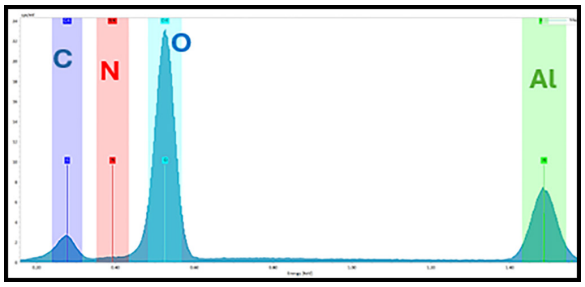

Figure 1: Cross-sectional EDX Spectrum of AAO Channels Post AlN ALD.

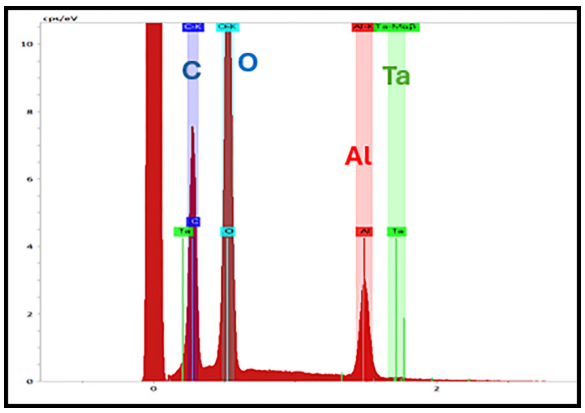

Figure 2: Cross-sectional EDX Spectrum of AAO Channels Post TaN ALD.

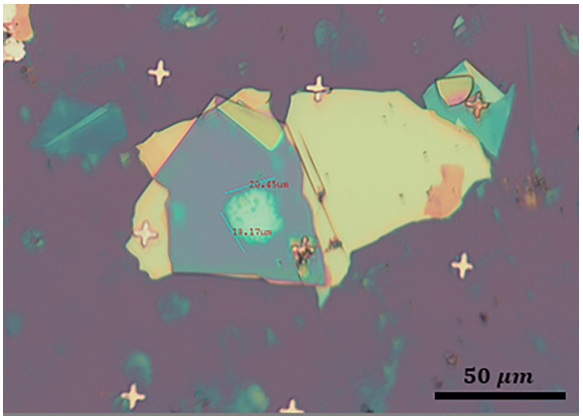

Figure 3: Optical Microscope Image of Compressed InBi Stack.

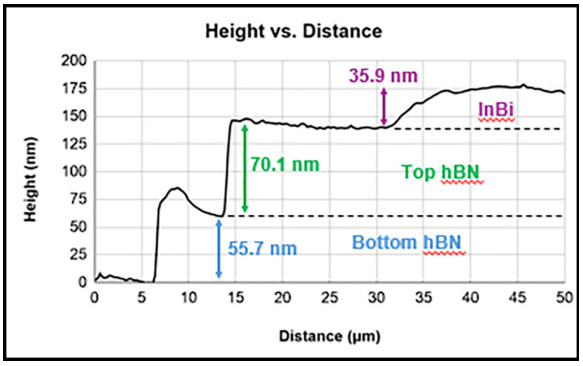

Figure 4: AFM Line Profile Graph of Compressed InBi Stack.

Micro-Additive Manufacturing Processes for Electrochemical CO_2 Reduction

CNF Summer Student: Hunter Saylor
Student Affiliation: Electrical and Computer Engineering, Morgan State University

Summer Program(s): 2024 Cornell NanoScale Science & Technology Facility Research Experience for Undergraduates Program with Morgan State University (CNF REU MSU)

Principal Investigator(s): Sadaf Sobhani, Mechanical and Aerospace Engineering, Cornell University

Mentor(s): Giancarlo D'Orazio, Mechanical and Aerospace Engineering, Cornell University

Program and Primary Source(s) of Research Funding: Cornell College of Engineering (CNF REU MSU), National Science Foundation under Grant No. NNCI-2025233 (CNF REU)

Contact: husay1@morgan.edu, sobhani@cornell.edu, gd373@cornell.edu

Summer Program Website: https://cnf.cornell.edu/education/reu/2024

Primary CNF Tools Used: Nanoscribe GT2, AJA Sputter, Zeiss Ultra SEM

Abstract:

This work investigates the application of micro-additive manufacturing in the development of gas diffusion electrodes (GDEs) for electrochemical CO2 reduction reactors. This technology relies on the principles of electrochemistry to convert CO2 into useful chemical products. A key focus of this work is the reactor design and fabrication, as these elements impact the overall efficiency and functionality of the system. The gas diffusion electrode is identified as a common failure point in such reactors. To enhance the performance and durability of the GDE, we utilize the Nanoscribe Photonic Professional GT2 two-photon lithography 3D printer to print a microporous layer atop a carbon paper electrode. This effort aims to mitigate electrolyte flooding in our vapor-fed reactor. A copper catalyst will be deposited onto the microporous layer using the AJA sputter system. Subsequent analysis of the GDE surface will be conducted using a scanning electron microscope (SEM) to ensure structural integrity and optimal surface characteristics. To evaluate the performance of the CO2 reduction reactor, measurements of open-circuit potential, electrochemical impedance spectroscopy, and cyclic voltammetry will be scrutinized. The results will highlight common failure modes, such as catalyst delamination and electrolyte flooding. Additionally, a long-duration, steady-state test will be performed to measure changes in potential at a fixed current, providing insights into the long-term performance and lifespan of the GDE. Our findings will deliver quantitative insights into the optimization of gas diffusion electrode synthesis, advancing the efficiency of electrochemical CO2 reduction processes. This research underscores the potential of micro-additive manufacturing in addressing critical challenges in renewable energy and carbon capture technologies.

Summary of Research:

In the effort to optimize the fabrication and design of the CO2 reduction reactor's Gas Diffusion Electrode (GDE), we addressed common failure modes such as catalyst degradation and flooding of the electrolyte into the vapor-fed reactor. To minimize these failure modes, we had to [1] characterize the reactor before and after long-duration trials, [2] design and print a microporous layer on the GDE, and [3] test the effect of electrolyte mixing into the reactor's expected liquid products.

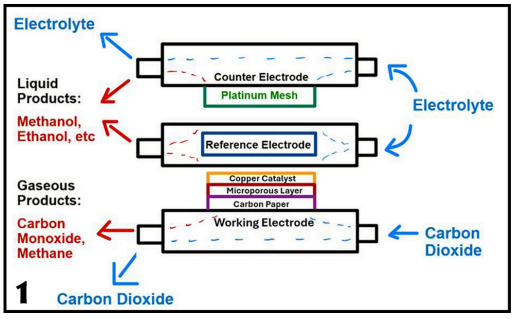

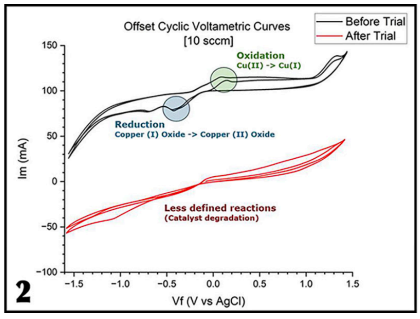

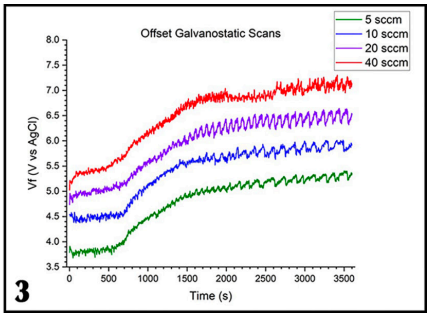

Figure 1, left: Diagram of CO2 reduction reactor. Figure 2, middle: Offset cyclic voltametric scans taken of reactor cell before and after long-duration trial. Figure 3, right: Offset galvanostatic scans of reactor cell at different CO2 flow rates.

The rate of degradation of the gas diffusion electrode's copper catalyst and the rate of flooding of electrolyte into the vapor-fed reactor are both dependent on the flow rate of CO2 into the reactor. In order to measure these effects, we employed the characterization of the reactor before and after an hour long run of the reactor at different flow rates. Our characterization involved taking cyclic voltametric scans of the reactor, in which a voltage is applied across the working and reference electrodes, and its current density is measured. These scans display the reduction and oxidation reactions occurring at the copper catalyst of the GDE. Over the course of the long-duration trial, a galvanostatic scan was taken, in which a steady current of 350 mA/cm^2 was applied and the voltage across the reactor was measured. The galvanostatic scan measures the rate of electrochemical reaction. Multiple trials were conducted at varying CO_2 flow rates of 5, 10, 20, and 40 standard cubic centimeters per minute (SCCM). The operating conditions in which we applied to our long-duration trials were influenced by previous literature, which concluded that 5 SCCM of CO_2 at an applied current density of 350 mA/cm^2 outputs the best reactor performance and efficiency [1].

3D-printing the microporous layer (MPL) offers control of the GDE's pore size and density. The MPL is printed on a layer of carbon paper using the Nanoscribe GT2, then a ~ 300 nm layer of copper is deposited on top of the MPL using AJA Sputter system. This design of the gas diffusion electrode allows the copper layer to be used as a catalyst for the CO_2 conversion, and the microporous layer to be used to prevent flooding of electrolyte into the vapor-fed reactor.

Another facet in the effort to optimize the design of the GDE involved measuring the effect that of electrolyte mixing into the liquid products of the CO_2 reduction reactor. To address this, we performed a test involving measuring the rise velocity of the various samples through a capillary tube. The samples included deionized water to act as a control, the electrolyte ($KHCO_3$), the alcohol and acid products, as well as the alcohol and acid products mixed with $KHCO_3$.

Conclusions and Future Steps:

The cyclic voltametric scans taken before and after the long-duration trials suggest that the copper catalyst degrades more rapidly if there is a higher CO_2 flow rate input.

This can be determined because the reduction and oxidation reactions that are present in the character-ization of the reactor before the long-duration trial are no longer present afterwards. The galvanostatic scans taken over the course of the trial also show that the CO_2 reduction reactor reaches steady-state operation after approximately half an hour.

Our 3D-printed microporous layer has pores approximately 1-5 microns in diameter, and also improves upon the previous method of 3D-printing the entire GDE. In comparison, printing the MPL takes ~ 6-9 hours, whereas printing the entire GDE takes ~ 35-55 hours.

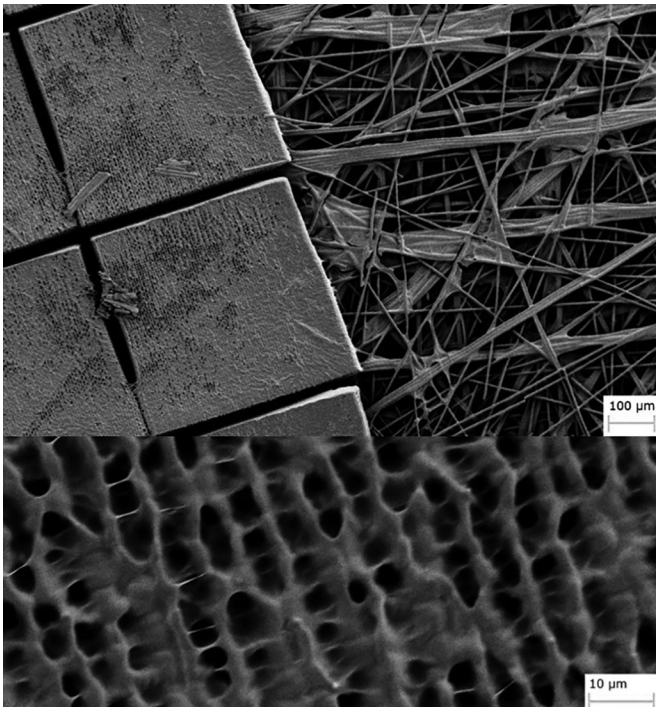

Figure 4: Scanning electron microscope (SEM) images of the microporous layer printed on carbon paper.

Results from measuring the rise velocity of electrolyte and liquid products through capillary tubes suggest that $KHCO_3$ has relatively low hydrophobicity, as it has the lowest rise velocity from our tests, and it lowers the rise velocity of the alcohol and acid products when they are mixed together. The results of these experiments will influence the hydrophobic coating used on the microporous layer.

Future work involves coating the printed microporous layer with a hydrophobic coating. The coated microporous layer will then be tested and its effectiveness against electrolyte flooding and catalyst degradation will be measured.

Acknowledgements:

Many thanks to 2024 Cornell NanoScale Facility Research Experience for Undergraduates Program with Morgan State University and the National Science Foundation Grant No. NNCI-2025233. Special thanks to my principal investigator Dr. Sadaf Sobhani for the wonderful opportunity, to my mentor Giancarlo D'Orazio for his patience and guidance, to my staff host Giovanni Sartorello for his support, and to Melanie-Claire Mallison for being an excellent host.

References:

[1] D. Corral, et al., "Advanced manufacturing for electrosynthesis of fuels and chemicals from CO2," Energy Environ. Sci., vol. 14, no. 5, pp. 3064-3074, May 2021, doi: 10.1039/D0EE03679J.

Study Unconventional Spin-Orbit Torque Generation on Micron-Sized Devices Fabricated with Photolithography

CNF Project Number: 598-96
Principal Investigator(s): Daniel C. Ralph
User(s): Xiaoxi Huang

Affiliation(s): Department of Physics, Cornell University

Primary Source(s) of Research Funding: Semiconductor Research Corporation-Superior Energy-efficient Materials and Devices

Contact: dcr14@cornell.edu, xh384@cornell.edu

Primary CNF Tools Used: DWL 66fs, AJA Sputter Deposition

Abstract:

Micron-sized devices made with DWL 66fs direct writer and AJA sputter system were used to study spin currents generated with magnetic ordering. We experimentally observed that antiferromagnetic ordering plays a significant role in enhancing spin current generation efficiency in $PdCrO_2$ thin films and canted magnetic moment produces out-of-plane damping-like torque in $SrRuO_3$ thin films.

Summary of Research:

Magnetic materials with perpendicular magnetic anisotropy (PMA) are the most promising materials for high-density magnetic memory; and the efficient magnetization switching of PMA-magnets are enthusiastically pursuit by Spintronics researchers, as it has the potential to realize energy-efficient high-density information storage. Fortunately, out-of-plane spin component borne by a spin current is theoretically predicted and experimentally demonstrated to be able to drive the efficient anti-damping switching of magnetization of a PMA-magnet [1]. Our primary research goal is to find materials that efficiently produce spin currents with out-of-plane spin component and ultimately demonstrate the efficient switching of magnetization of PMA-magnet pillars with diameters as small as 100 nm. Our search for such materials has been centered around materials that have magnetic orderings, including both ferromagnetic and anti-ferromagnetic orderings.

Two successful trials have been made on $PdCrO_2$, which an anti-ferromagnet below 37 K, and $SrRuO_3$, which is a ferromagnet below 150 K. To detect spin current generation and the specific spin orientations allowed in these materials, micron-sized devices such as spin-torque ferromagnetic resonance (ST-FMR) devices and Hall bar devices are patterned on these materials.

The devices for ST-FMR and Hall measurements-established techniques for spin-orbit torque characterization [2] is shown in Figure 1 and Figure 2. Bar structures with dimensions of

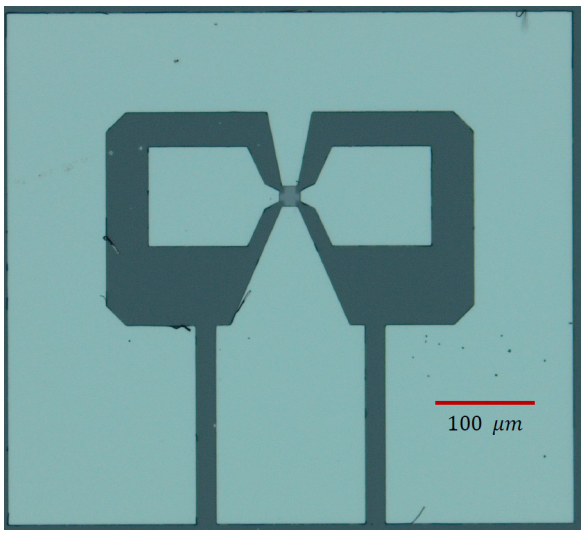

Figure 1: Spin torque ferromagnetic resonance device.

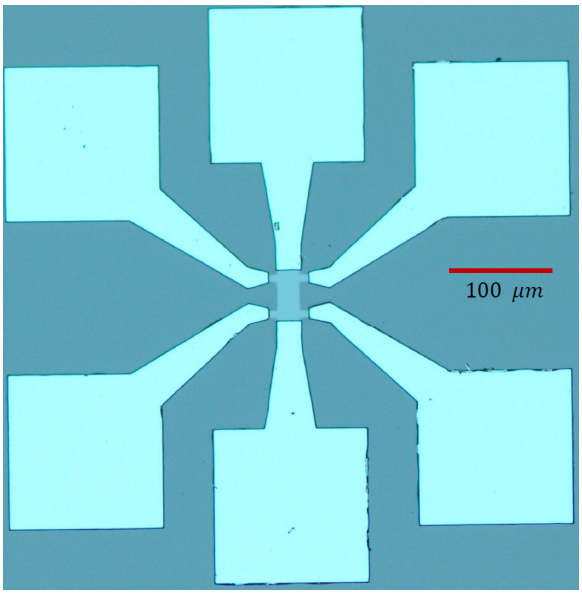

Figure 2: Hall device for second Harmonic Hall measurements.

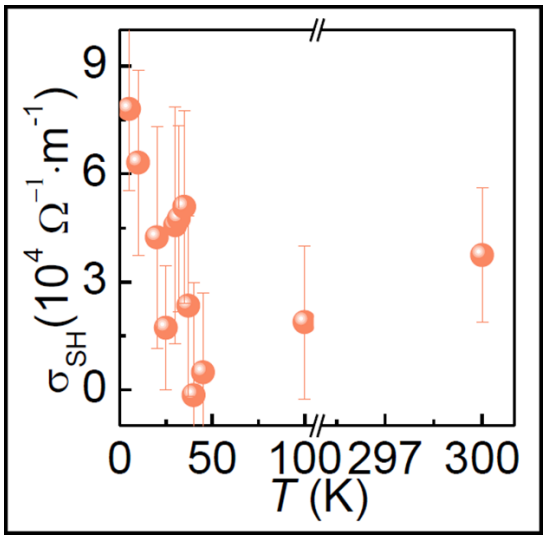

Figure 3: Spin Hall conductivity as a function of temperature for a 2 nm $PdCrO_2$ thin film.

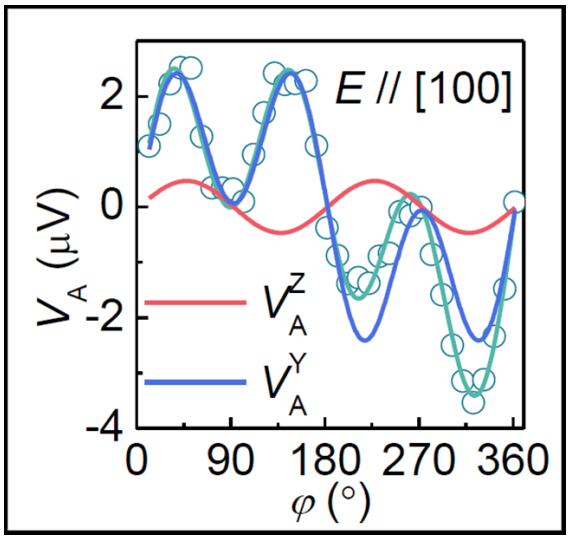

Figure 4: The anti-symmetric component of the mixing voltage for a 5 nm $SrRuO_3$ sample. The device is oriented parallel to [100] direction in the plane and the measurements were carried out at 110 K.

10 x 40μm and 20 x 70μm are patterned with Heidelberg DWL 66fs laser direct writer. Then contacts made of Ti/Pt were deposited on the patterns in an AJA sputtering system. Spin current generation in $PdCrO_2$ were successfully detected with such devices; and the spin current generation efficiency as a function of temperature in $PdCrO_2$ is shown in Figure 3. A strong dependence of spin current generation on temperature is observed. Intriguingly, a strong upturn of spin current generation efficiency is seen at approximately the Neel temperature of $PdCrO_2$, implying the critical role that antiferromagnetic ordering plays in generating spin currents.

A manuscript on this work has been composed and is to be submitted soon. Another example on spin current generated with magnetic ordering is unconventional spin-orbit torque generation in $SrRuO_3$. $SrRuO_3$ thin films when grown on (001)-oriented $SrTiO_3$ substrates are shown to exhibit canted magnetization and ferromagnets with magnetic moment canted out of the plane are predicted to be able to produce tilted spin currents with tilted spin polarization [3]. The spin-orbit torque generation in $SrRuO_3$ is conducted on ST-FMR devices (Figure 1). When the rf current and oscillating magnetoresistance are mixed together, a dc mixing voltage is produced.

The anti-symmetric component of the mixing voltage is contributed by the out-of-plane torques. The fitting of the anti-symmetric voltage detected in $SrRuO_3$ thin films requires a *sin*2φ component (Figure 4), which is the signature of the out-of-plane damping like torque produced by the out-of-plane component of the spin polarization. This is the most exciting and important finding of our work so far and we are actively preparing a manuscript on this matter.

Conclusions and Future Steps:

Magnetic ordering plays a crucial role in either enhancing spin current generation or producing out-of-plane damping-like torques. We anticipate finishing characterizing the unconventional spin-orbit torque generation in these materials and start demonstrating magnetization switching PMA-magnetic nano-pillars.

References:

[1] David MacNeill, et al., Nat. Phys. 13, 300 (2017).

[2] Luqiao Liu, et al., Science 336, 555 (2012).

[3] Tomohiro Taniguchi, et al., Phys. Rev. Lett. 3, 044001 (2015).

Van der Waals Magnetic Tunnel Junctions with Metallic Transition Metal Dichalcogenide Electrodes

CNF Project Number: 598-96
Principal Investigator(s): Daniel Ralph
User(s): Bozo Vareskic

Affiliation(s): Laboratory for Atomic and Solid State Physics, Cornell University

Primary Source(s) of Funding: Air Force Office of Scientific Research

Contact: dcr14@cornell.edu, bv227@cornell.edu

Primary CNF Tools Used: Heidelberg DWL-2000, GCA-AS200 i-line stepper, SC4500 Even/Odd-Hour Evaporator

Abstract:

Magnetic tunnel junctions (MTJs) are a useful platform for studying electrically insulating van der Waals magnets. The evolution of the tunneling current as a function of junction bias and applied external magnetic field has been shown to reveal information about the nature of interlayer exchange, spin-filtering, and two dimensional magnons [1-3]. These previous studies have employed few layer graphene for contact electrodes. Theoretical work [4], however, suggests that by replacing few layer graphene with a metallic transition metal dichalcogenide (TMD), the junction impedance can be lowered and the magnetoresistance increased, making the junctions more favorable for spintronic applications. Here, we fabricate MTJs where the barrier layer is antiferromagnetic $CrCl_3$ and the junction electrodes are $TaSe_2$ and measure the tunneling characteristics as a function of applied magnetic field.

Summary of Research:

$CrCl_3$ is a layered van der Waals magnet where each individual layer hosts ferromagnetic exchange interactions between neighboring spins while adjacent layers couple antiferromagnetically. The moments are pointed in the plane of the layers with no anisotropy within the plane. The weak interlayer coupling allows for the net magnetic moment to be manipulated by an external magnetic field. Previous studies with few layer graphene/$CrCl_3$/few layer graphene junctions have shown that the tunneling current is sensitive to the orientation of the layer magnetic moments relative to one another [1-3]. However, spintronics applications where the tunneling current can be used as a readout of the magnetic state will require lower impedance junctions.

First principles density functional theory calculations indicate that due to more favorable band alignment and higher density states that junctions with electrodes of metallic transitional metal dichalcogenides host larger junction conductivity and magnetoresistance compared to junctions with graphitic electrodes [4].

We fabricate $TaSe_2/CrCl_3/TaSe_2$ junctions by exfoliating all materials in an inert glove box environment to avoid exposure to ambient oxygen and water. The junction is encapsulated in hexagonal boron nitride from above and below and then transferred to prepatterned metallic electrodes that were prepared with the Heidelberg Mask Writer DWL-2000, GCA-AS200 i-line stepper, and SC4500 Even/Odd-Hour Evaporator. Figures 1 and 2 show a device schematic and micrograph, respectively.

Transport measurements are performed at $T = 2\ K$ by applying a DC bias voltage and measuring the resulting DC tunneling current. All external magnetic fields are applied in the plane of the device. Figure 3 shows the current voltage characteristic of the junction at $B = 0\ T$ and $B = 2\ T$. As the externally applied field is increased, the moments of the individual layers will reorient themselves and approach a parallel configuration to minimize energetic contributions from interlayer exchange and Zeeman effects. At $B = 2\ T$, due to spin filtering, this configuration will have a lower tunneling barrier and thus, a lower threshold voltage for the onset of Fowler-Nordheim tunneling than the antiparallel configuration at $B = 0\ T$.

We then apply a constant DC bias of $V = 1.25\ V$ and measure how the tunneling current evolves as a function of applied magnetic field. The tunneling current increases with an applied field as the moments evolve from antiparallel towards a parallel configuration. This

is consistent with the lowering of the tunneling barrier with increasing magnetic field via the spin filtering effect. The magnetoresistance is defined as

$$MR = 100 \times \frac{I(B) - I(B=0\,T)}{I(B=0\,T)},$$

and we measure a magnetoresistance of ~ 150%. Future work will involve exploring different metals as electrode layers and fabricating devices suitable for four-point measurements to avoid contributions from contact resistance.

References:

[1] Klein, D. R., et al. Probing magnetism in 2D van der Waals crystalline insulators via electron tunneling. Science 360, 1218 (2018).

[2] Wang, Z., et al. Determining the phase diagram of atomically thin layered antiferromagnet $CrCl_3$. Nature Nano. 14, 1116 (2019).

[3] Cai, X., et al. Atomically thin $CrCl_3$: An in-plane layered antiferromagnetic insulator. Nano Letters 19, 3993 (2019).

[4] Heath, J. J., et al. Spin injection enhancements in van der Waals magnetic tunnel junctions through barrier engineering. Phys. Rev. Applied 16, L041001 (2021).

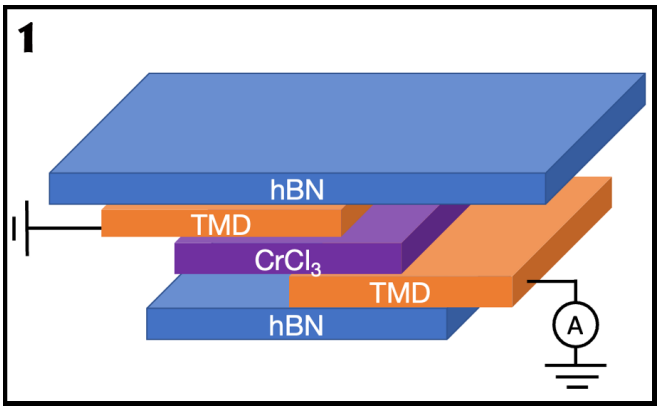

Figure 1: Device schematic of $TaSe_2/CrCl_3/TaSe_2$ magnetic tunnel junction. Hexagonal boron nitride is used to encapsulate the $CrCl_3$ to prevent degradation from ambient oxygen and water.

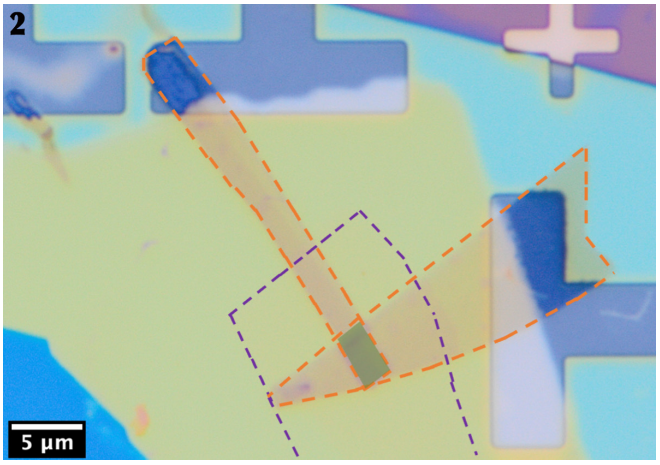

Figure 2: Micrograph of $TaSe_2/CrCl_3/TaSe_2$ magnetic tunnel junction. The $TaSe_2$ and $CrCl_3$ layers are outlined with the dashed orange and purple lines respectively. Scale bar: 5 µm.

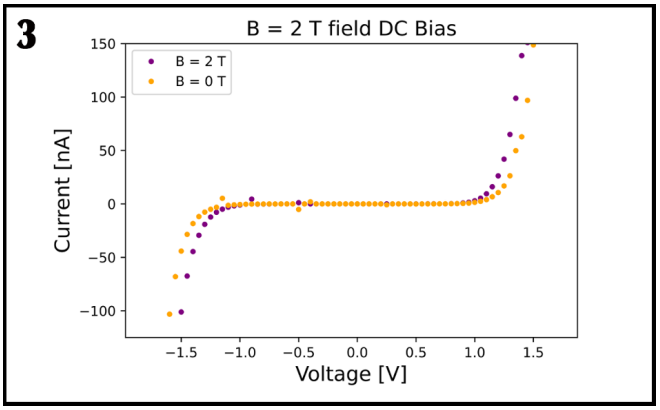

Figure 3: Tunneling current as a function of applied DC bias. The tunneling current at B = 0 T is orange and at B = 2 T is purple. Measurements are performed at T = 2 K, and the magnetic field is applied in the plane.

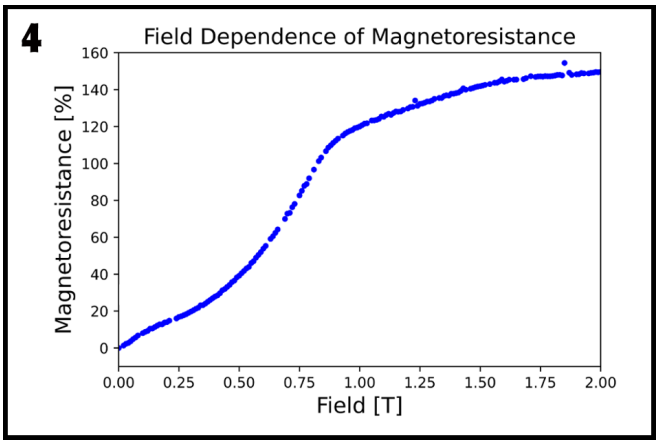

Figure 4: Magnetoresistance as a function of in-plane magnetic field. A constant DC bias of V =1.25 V is applied. The tunneling current increases as the moments of the individual layers approach a parallel configuration.

Nanofabricated Superconducting Devices for Vortex Dynamics and Qubits

CNF Project Number: 1314-05
Principal Investigator(s): Britton L.T. Plourde
User(s): Brad Cole, Kenneth Dodge, Clayton Larson, Eric Yelton

Affiliation(s): Department of Physics, Syracuse University

Primary Source(s) of Research Funding: Army Research Office

Contact: bplourde@syr.edu, bgcole@syr.edu, krdodgej@syr.edu, cllarson@syr.edu, epyelton@syr.edu

Primary CNF Tools Used: ASML Photostepper, JEOL 6300, Plasma-Therm 770

Abstract:

We fabricate superconducting microwave devices for studying the dynamics of vortices at low temperatures and for forming novel qubits. Vortices are quantized bundles of magnetic flux that thread many different superconductors over a particular range of applied magnetic field. By using disordered superconducting thin films to form high kinetic inductance wires combined with novel arrays of Josephson junctions, we are able to build structures that can lead to qubits that are topologically protected against decoherence. With charge-sensitive superconducting qubits, we are able to probe sources of correlated errors in quantum processors.

Summary of Research:

Superconducting microwave circuits play an important role in quantum information processing. Circuits composed of Josephson junctions and capacitors with superconducting electrodes can serve as qubits, the fundamental element of a quantum computing architecture. Various loss mechanisms limit the ultimate performance of these devices, including trapped magnetic flux vortices. Vortices can be trapped in the superconducting electrodes when background magnetic fields are present and contribute dissipation when driven with microwave currents [1]. Thus, techniques for controlling the trapping of vortices are critical to the development of large-scale quantum information processors with superconducting circuits.

By arranging nanoscale Al-AlOx-Al Josephson tunnel junctions in novel arrays, it is possible to implement new qubit designs that are protected against decoherence [2-4]. We are also able to use such Al-AlOx-Al tunnel junctions in superconducting qubits to probe poisoning effects from nonequilibrium quasiparticles, which are a source of correlated errors in quantum processors. We can mitigate this quasiparticle poisoning through the use of electroplated Cu metallic reservoirs for downconversion of high energy phonons [5].

We fabricate our microwave resonators from various superconducting films, including aluminum and niobium, deposited onto silicon wafers in vacuum systems at Syracuse University. We define the patterns on the ASML stepper and transfer them into the films with a combination of reactive ion etching and liftoff processing. For defining Josephson junctions, we use the JEOL 6300 along with a dedicated deposition system at Syracuse University. We measure these circuits at temperatures of 100 mK and below in our lab at Syracuse University.

References:

[1] Song, C., Heitmann, T.W., DeFeo, M.P., Yu, K., McDermott, R., Neeley, M., Martinis, John M., Plourde, B.L.T.; "Microwave response of vortices in superconducting thin films of Re and Al"; Physical Review B 79, 174512 (2009).

[2] Doucot, B., Ioffe, L.; "Physical implementation of protected qubits"; Reports on Progress in Physics 75, 072001 (2012).

[3] Cole, B., Dodge, K., Liu, Y., Shearrow, A., Snyder, M., Klots, A., Ioffe, L., McDermott, R., Plourde, B.; "Electronic capacitance in tunnel junctions for protected charge-parity qubits"; Bull. Am. Phys. Soc. 2024, https://meetings.aps.org/Meeting/MAR24/Session/N48.3

[4] Dodge, K., Liu, Y., Klots, A., Cole, B., Shearrow, A., Senatore, M., Zhu, S., Ioffe, L., McDermott, R., Plourde, B.; "Hardware implementation of quantum stabilizers in superconducting circuits"; Physical Review Letters 131, 150602 (2023).

[5] Iaia, V., Ku, J., Ballard, A., Larson, C.P., Yelton, E., Liu, C.H., Patel, S., McDermott, R., Plourde, B.L.T.; "Phonon downconversion to suppress correlated errors in superconducting qubits"; NatureCommunications 13, 6425 (2022).

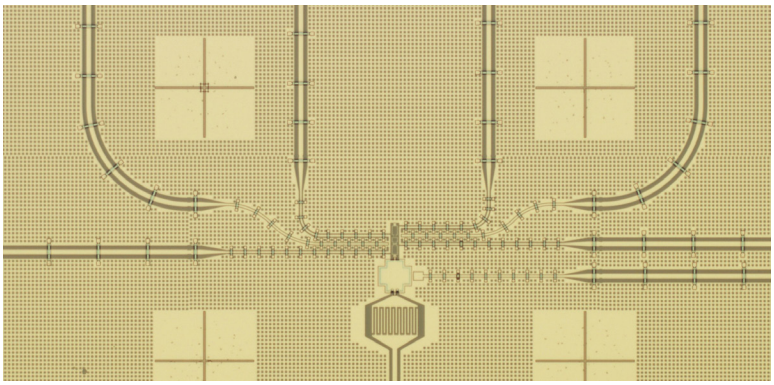

Figure 1: Optical micrograph of topologically protected superconducting quantum circuit.

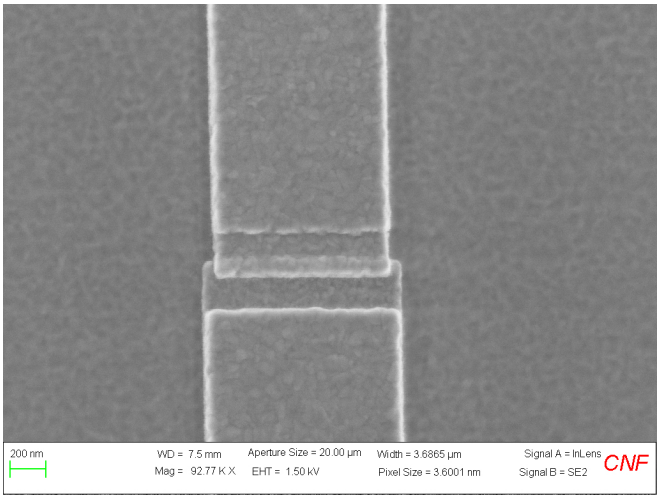

Figure 2: SEM image of Al-AlOx-Al Josephson tunnel junction for superconducting qubit.

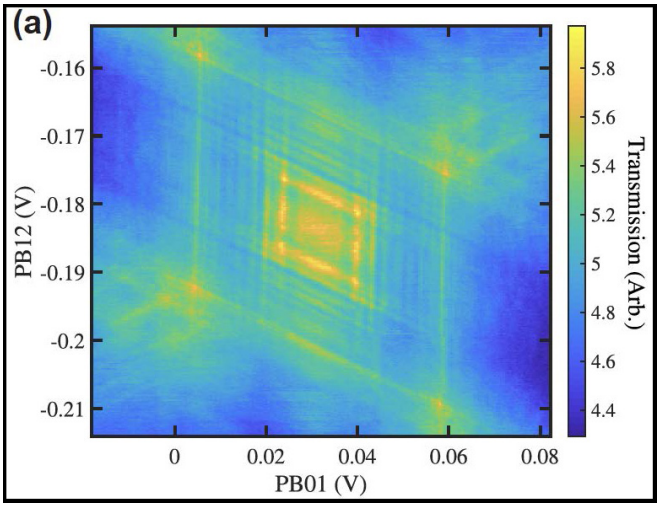

Figure 3: Measurement of microwave readout cavity modulation with magnetic flux using on-chip controllines coupled to topologically protected superconducting circuit.

Fabrication of Nanoscale Josephson Junctions for Quantum Coherent Superconducting Circuits

CNF Project Number: 1735-08
Principal Investigator(s): Britton L.T. Plourde
User(s): Brad Cole, Tianna McBroom, J.T. Paustian

Affiliation(s): Department of Physics, Syracuse University

Primary Source(s) of Research Funding: Air Force Research Lab, Air Force Office of Scientific Research

Contact: bplourde@syr.edu, bgcole@syr.edu, tamcbroo@syr.edu, jtpausti@syr.edu

Primary CNF Tools Used: ASML Photostepper, JEOL 6300, Plasma-Therm 770

Abstract:

We fabricate nanoscale superconductor tunnel junctions and other structures for experiments involving quantum coherent circuits. Such circuits have shown great promise in recent years for explorations of quantum mechanics at the scale of circuits on a chip and for forming qubits, the foundational elements of a quantum computer. The quantum state of these superconducting qubits can be manipulated with microwave radiation at low temperatures. We are currently developing superconducting metamaterial structures with novel microwave mode spectra for coupling to superconducting qubits.

Summary of Research:

The unique properties of nanoscale Josephson junctions enable a wide range of novel superconducting circuits for investigations in many diverse areas. In recent years, circuits composed of such junctions have emerged as promising candidates for the element of a quantum computer, due to the low intrinsic dissipation from the superconducting electrodes and the possibility of scaling to many such qubits on a chip [1]. The quantum coherent properties of the circuits are measured at temperatures below 50 mK with manipulation of the qubit state through microwave excitation.

We are developing multimode microwave resonators using combinations of superconducting lumped-circuit elements to engineer metamaterial transmission lines, including metamaterial ring resonator devices. These structures exhibit novel mode structures characteristic of left-handed materials [2]. We are fabricating such metamaterial transmission lines from Al and Nb films on Si and characterizing these at low temperatures [2]. We are working on experiments to couple these left-handed lines and ring resonators to superconducting qubits for experiments involving the exchange of microwave photons [2-4].

In addition to multimode systems, we also fabricate and measure superconducting coplanar waveguide (CPW) microwave resonators to probe loss mechanisms that limit quality factors at low temperatures. Such resonator measurements serve as a proxy for characterizing decoherence sources in superconducting qubits. We also use CPW resonators to probe the microwave loss contributions from magnetic flux vortices in superconducting films [5].

We pattern these circuits at the CNF with nanoscale structures defined with electron-beam lithography on the JEOL 6300 integrated with photolithographically defined large-scale features. The junctions are fabricated using the standard double-angle shadow evaporation technique, in which a resist bilayer of copolymer and PMMA is used to produce a narrow PMMA airbridge suspended above the substrate. Evaporation of aluminum from two different angles with an oxidation step in between forms a small Al-AlOx-Al tunnel junction from the deposition shadow of the airbridge. We have developed a process for defining these junctions with electron-beam lithography and we perform the aluminum evaporations in a dedicated chamber at Syracuse. We pattern large-scale features using the ASML stepper, with electron-beam evaporation of Al and sputter-deposition of Nb. Measurements of these circuits are performed in cryogenic systems at Syracuse University, including dilution refrigerators for achieving temperatures below 30 mK.

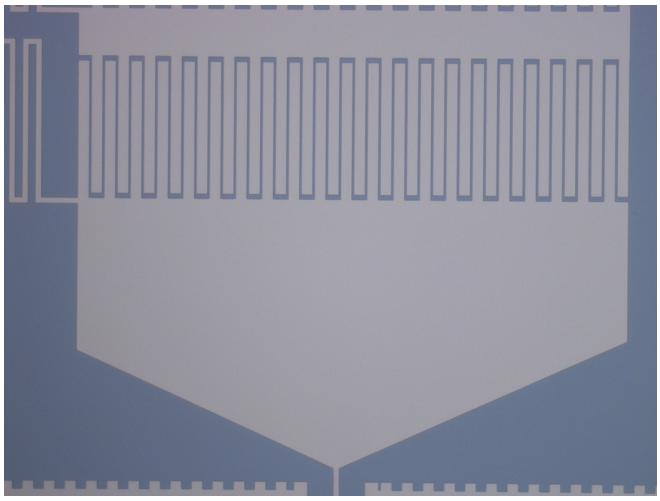

Figure 1: Optical micrograph of interdigitated capacitor in left-handed metamaterial ring resonator fabricated from Nb on Si.

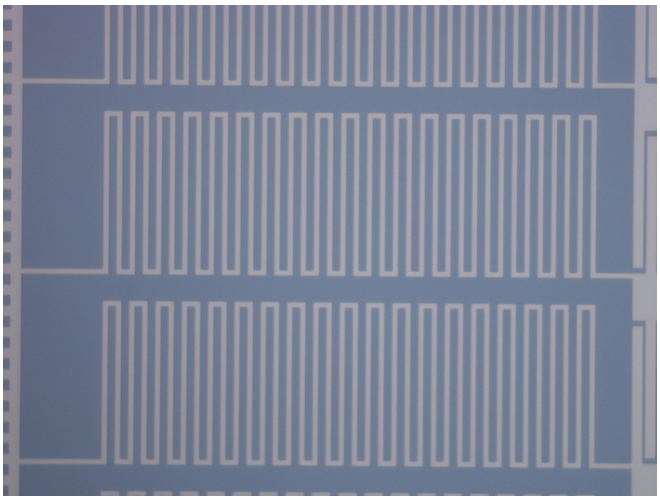

Figure 2: Optical micrograph of meander-line inductors in left-handed metamaterial ring resonator fabricated from Nb on Si.

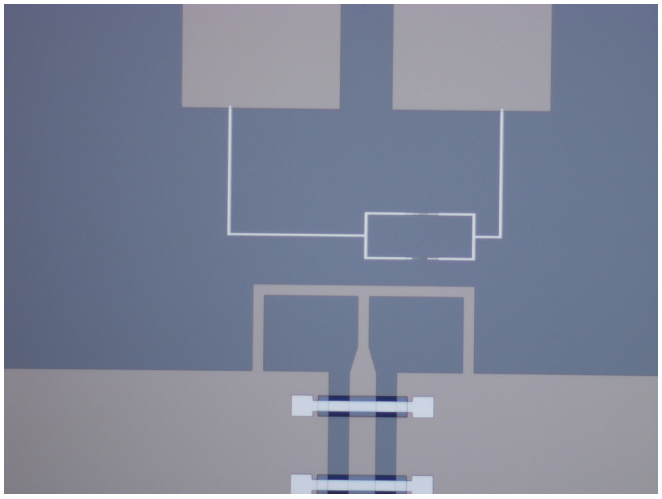

Figure 3: Zoomed-in optical micrograph of transmon qubit with Al-AlOx-Al junctions and Nb capacitor pads coupled to metamaterial transmission-line resonator with on-chip Nb flux-bias line.

References:

[1] Clarke, J. and Wilhelm, F.K.; "Superconducting quantum bits"; Nature, 453, 1031 (2008).

[2] Wang, H., Zhuravel, A., Indrajeet, S., Taketani, B., Hutchings, M., Hao, Y., Rouxinol, F., Wilhelm, F., LaHaye, M.D., Ustinov, A., Plourde, B.; "Mode Structure in Superconducting Metamaterial Transmission Line Resonators"; Physical Review Applied 11, 054062 (2019).

[3] Indrajeet, S., Wang, H., Hutchings, M.D., Taketani, B.G., Wilhelm, F.K., LaHaye, M.D., Plourde, B.L.T.; "Coupling a Superconducting Qubit to a Left-Handed Metamaterial Resonator"; Physical Review Applied 14, 064033 (2020).

[4] McBroom, T.A., Schlabes, A., Xu, X., Ku, J., Cole, B.G., Indrajeet, S., LaHaye, M., Ansari, M., Plourde, B.; "Entangling Interactions Between Artificial Atoms Mediated by a Multimode Left-Handed Superconducting Ring Resonator"; Physical Review X Quantum 5, 020325 (2024).

[5] Paustian, JT, Larson, C., Dodge, K., Plourde, B.; "Vortex viscosity in superconducting granular aluminum resonators"; Bull. Am. Phys. Soc. 2024, https://meetings.aps.org/Meeting/MAR24/Session/N47.13.

Realization of the Haldane Chern Insulator in a Moiré Lattice

CNF Project Number: 2633-18
Principal Investigator(s): Jie Shan, Kin Fai Mak
User(s): Wenjin Zhao, Kaifei Kang, Yichi Zhang, Zui Tao, Lizhong Li, Charles Tschirhart

Affiliation(s): Kavli Institute at Cornell for Nanoscale Science, Laboratory of Atomic and Solid State Physics, School of Applied and Engineering Physics; Cornell University

Primary Source(s) of Research Funding: DOE, NSF, AFOSR

Contact: jie.shan@cornell.edu, kinfai.mak@cornell.edu, wz435@cornell.edu, kk726@cornell.edu, yz2662@cornell.edu, zt227@cornell.edu, ll646@cornell.edu, ct638@cornell.edu

Primary CNF Tools Used: Zeiss Supra SEM, Nabity Nanometer Pattern Generator System (NPGS), SC4500 Odd/Even-Hour Evaporator, Autostep i-line Stepper, Hamatech Wafer Processor Develop, Heidelberg Mask Writer - DWL2000, Photolithography Spinners, Dicing Saw - DISCO

Abstract:

The Chern insulator displays a quantized Hall effect without Landau levels. Theoretically, this state can be realized by engineering complex next-nearest-neighbor hopping in a honeycomb lattice — the so-called Haldane model [1]. We realize a Haldane Chern insulator in AB-stacked $MoTe_2/WSe_2$ moiré bilayers, which form a honeycomb moiré lattice with two sublattices residing in different layers [2]. We show that the moiré bilayer filled with two holes per unit cell is a quantum spin Hall insulator with a tunable charge gap. Under a small out-of-plane magnetic field, it becomes a Chern insulator with a finite Chern number because the Zeeman field splits the quantum spin Hall insulator into two halves of opposite valley — one with a positive and the other a negative moiré band gap. We also demonstrate experimental evidence of the Haldane model at zero external magnetic field by proximity coupling the moiré bilayer to a ferromagnetic insulator.

Summary of Research:

When a two-dimensional electron gas is exposed to high magnetic fields, it forms Landau levels, and quantized Hall conductance is observed [3]. Researchers aim to achieve a quantum Hall state without external magnetic fields, known as a Chern insulator [1]. These insulators have been realized in a few materials, such as magnetic topological insulators and moiré materials. A proposed method involves transforming a quantum spin Hall (QSH) insulator into a Chern insulator through magnetic interactions [4].

In this study, we use AB-stacked $MoTe_2/WSe_2$ moiré bilayer, which is a new QSH insulator with a tunable charge gap and unique spin-valley-layer locking. By applying an out-of-plane magnetic field or proximity coupling to a ferromagnetic insulator, the material transitions into a Chern insulator. This transformation is facilitated by valley-dependent magnetic interactions and Zeeman energies. We demonstrated that an out-of-plane magnetic field of about 1 Tesla or proximity coupling can induce this transition. We investigated the transport properties of these bilayers, showing the emergence of a nearly quantized Hall resistance for the Chern insulator state at specific electric and magnetic field conditions. The results support the realization of a Haldane Chern insulator and suggest a new method for creating Chern insulators through tunable band inversion and magnetic proximity effects.

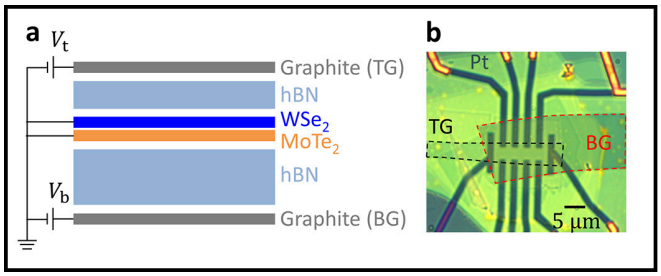

Figure 1: a, Device schematics. b, Optical microscope image of a dual-gated device. The scale bar is 5 µm.

Figure 1 shows the schematic and optical image of a device. We fabricated dual-gated $MoTe_2/WSe_2$ devices using a layer-by-layer dry-transfer technique. We deposited 5-nm Pt contacts on hBN by standard electron-beam lithography and evaporation, followed by another step of electron-beam lithography and metallization to form a bilayer of 5-nm Ti and 40-nm Au to connect the thin Pt contacts on hBN to pre-patterned electrodes.

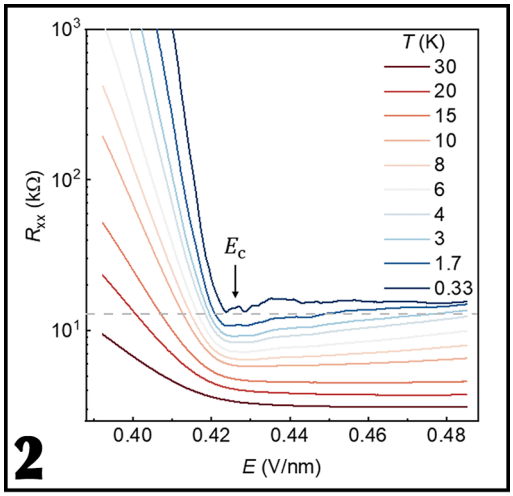

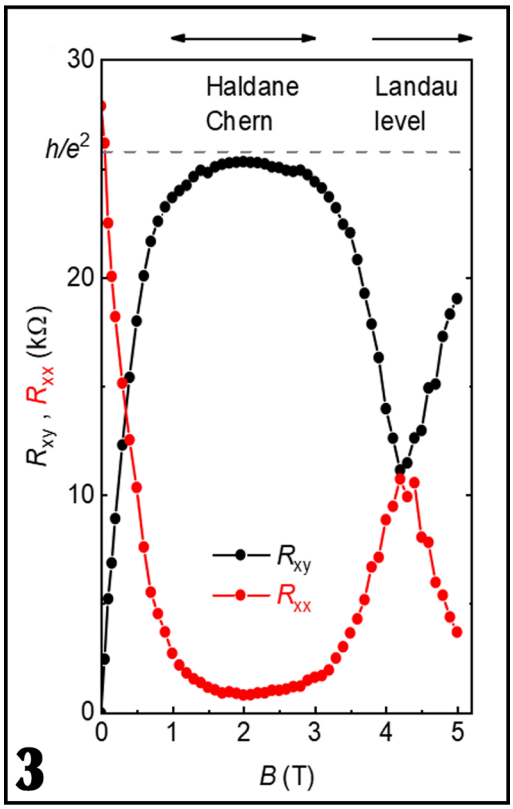

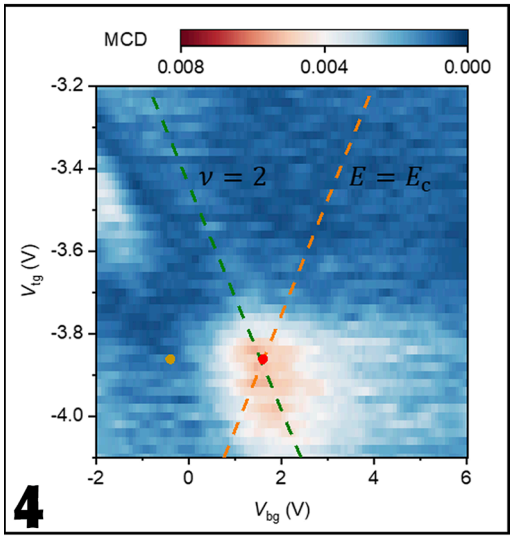

Figure 2 shows the electric-field dependence of R_{xx} at $\nu = 2$ and temperature $T = 0.33$-30 K. The resistance shows a minimum near E_c and distinct behaviors on two sides of E_c. Below E_c, R_{xx} decreases as E approaches E_c; and at a fixed field, R_{xx} diverges as T decreases. This is a typical response of an insulator with a diminishing band gap towards E_c. Above E_c, R_{xx} plateaus, and the value saturates around 15 kΩ $\approx 1.16\ h/2e^2$ at 0.33 K. The nearly quantized R_{xx} plateau suggests the emergence of a QSH insulator for $E > E_c$, where E_c corresponds to the quantum critical point for band inversion.

Figure 3 is the magnetic-field dependence of R_{xy} and R_{xx} to show this transition from the QSH insulator to the Haldane Chern insulator. The Hall resistance increases sharply from 0 at $B = 0$ T, plateaus between 1 T and 3 T, and displays non-monotonic field dependence for $B >$ 3 T. The plateau value (≈ 25.4 kΩ) is within 2% of the quantized Hall resistance, h/e^2. Concurrently, R_{xx} drops sharply with increasing field and remains small (< 1 kΩ) between 1 T and 3 T. Hence, when we set E near the band inversion critical point, a moderate magnetic field between 1 T and 3 T is sufficient to induce the Chern state.

Figure 4 shows the gate voltage dependence of the spontaneous magnetic circular dichroism (MCD) of a $CrBr_3$-$MoTe_2$/WSe_2 device, where the $CrBr_3$ is a ferromagnetic insulator. The observed MCD hot spot demonstrates spontaneous time reversal symmetry breaking near the band inversion critical point. This is consistent with the emergence of an exchange field from the magnetic proximity effect at the $CrBr_3$-$MoTe_2$/WSe_2 interface. Similar to the external magnetic field, the proximity exchange field splits the QSH insulator near band inversion to the Haldane model.

Conclusion and Future Steps:

We have realized a Haldane Chern insulator in AB-stacked $MoTe_2$/WSe_2 moiré bilayers. Our study presents a generic route to realizing Chern insulators through tunable band inversion and magnetic proximity coupling. The demonstrated large exchange field has the potential to stabilize a large-gap Chern insulator. Future transport studies with improved electrical contacts are required to further establish the Haldane physics under zero magnetic field.

References:

[1] Haldane, F. D. M. Phys. Rev. Lett. 61, 2015-2018 (1988).

[2] Li, T., et al. Nature 600, 641-646 (2021).

[3] Klitzing, K. V., Dorda, G., and Pepper, M. Phys. Rev. Lett. 45, 494-497 (1980).

[4] Liu, C., et al. Quantum Wells. 101, 146802 (2008).

Figure 2, top: Electric-field dependence of R_{xx} at $\nu = 2$ at different temperatures. Figure 3, middle: Magnetic-field dependence of R_{xx} and R_{xy} at $\nu = 2$ and $E = E_c$. The lines are guides to the eye. The Hall resistance is nearly quantized at h/e^2 (dashed line) between 1 T and 3 T. It is divided into the low-field (Haldane Chern) and high-field (Landau level) regimes. Figure 4, bottom: Spontaneous MCD of the $CrBr_3$-$MoTe_2$/WSe_2 device as a function of the top and bottom gate voltages. The dashed lines denote constant filling factor $\nu = 2$ (green lines) and constant electric field $E = E_c$ (orange lines).

Giant Spin Hall Effect in AB-Stacked $MoTe_2/WSe_2$ Bilayers

CNF Project Number: 2633-18
Principal Investigator(s): Jie Shan, Kin Fai Mak
User(s): Zui Tao, Bowen Shen, Wenjin Zhao, Tingxin Li, Shengwei Jiang, Lizhong Li

Affiliation(s): Laboratory of Atomic and Solid State Physics, School of Applied and Engineering Physics, Kavli Institute at Cornell for Nanoscale Science; Cornell University

Primary Source(s) of Research Funding: DOE, NSF, AFOSR

Contact: jie.shan@cornell.edu, kinfai.mak@cornell.edu, zt227@cornell.edu, bs792@cornell.edu, wz435@cornell.edu, tl684@cornell.edu, sj538@cornell.edu, ll646@cornell.edu

Primary CNF Tools Used: Zeiss Supra SEM, Nabity Nanometer Pattern Generator System (NPGS), SC4500 Odd/Even-Hour Evaporator, Autostep i-line Stepper, Hamatech Wafer Processor Develop, Heidelberg Mask Writer - DWL2000, Photolithography Spinners, Dicing Saw - DISCO

Abstract:

The spin Hall effect (SHE) [1,2], in which an electrical current generates a transverse spin current, plays an important role in spintronics for the generation and manipulation of spin-polarized electrons. The phenomenon originates from spin-orbit coupling. In general, stronger spin-orbit coupling favors larger SHEs but shorter spin relaxation times and diffusion lengths. Achieving large SHEs and long-range spin transport simultaneously in a single material has remained a challenge [3]. Here we demonstrate a giant intrinsic SHE that coexists with ferromagnetism in TMD moiré bilayers by direct magneto optical imaging. We also observe long-range spin Hall transport and efficient non-local spin accumulation limited only by the device size (about 10 μm). Our results demonstrate moiré engineering of Berry curvature and electronic correlations for potential spintronics applications.

Summary of Research:

In this study, we explore the intrinsic SHE in AB-stacked $MoTe_2/WSe_2$ bilayers (where the two monolayer crystals are twisted by about 180° and a moiré pattern with a period of about 5 nm due to the lattice mismatch is formed) [4]. The SHE, critical for spintronics, is typically enhanced by strong spin-orbit coupling, but the strong spin-orbit coupling also tends to shorten the spin relaxation times and diffusion lengths. It is therefore challenging to achieve large SHEs and long-range spin transport in a single material. We demonstrate that by using moiré engineering, these properties can be achieved simultaneously. We observe spin accumulation on transverse sample edges that nearly saturates the spin density under moderate electrical currents with density < 1 A/m. We also observe long-range spin Hall transport, as demonstrated by the extended spin current distribution profile. The giant SHE is observed near the interaction-driven Chern insulating state (with one hole per moiré unit cell) and emerges after the quantum anomalous Hall (QAH) breakdown and at low temperatures. Our results highlight the potential of moiré engineering for creating Berry curvature hotspots and controlling electronic correlations. The demonstration of giant SHEs in the same material platform as many reported exotic quantum many-body phenomena opens exciting opportunities for gate-defined lateral heterostructure quantum devices.

Figure 1 is the typical setup for spin Hall effect measurements. A bias current along the x-axis induces a spin Hall current along the y-axis. We fabricated dual-gated AB-stack $MoTe_2/WSe_2$ devices using the reported layer-by-layer dry-transfer technique [5]. Few-layer graphite and hexagonal boron nitride (hBN) are used as the gate electrode and gate dielectric, respectively, in both the top and bottom gates. We first deposited 5 nm Pt contacts on the bottom gate hBN by standard electron-beam lithography and evaporation. We then performed another step of electron-beam lithography and metallization to deposit 5 nm Ti/40-nm Au which connects the thin Pt contacts on hBN to pre-patterned electrodes on the Si substrate.

We transferred the $MoTe_2/WSe_2$ moiré bilayers on top of the hBN layer such that the Pt electrodes are in direct contact with the $MoTe_2/WSe_2$ moiré. Figure 1b shows an optical microscope image of a multi-terminal Hall bar device. The scale bar represents 5 μm.

Figure 2 shows the giant spin accumulation and QAH breakdown. Bias current-dependent MCD images at 6 K (Figure 2a) and 1.6 K (Figure 2b) were taken at the center of the QAH region in the filling-displacement phase diagram. The black dashed lines mark the sample

boundaries, and the arrows show the bias current direction. Zero-bias spontaneous MCD is observed only at 1.6 K. The high-bias MCD images, which consist of two domains, are nearly identical for 1.6 K and 6 K. To analyze the interplay between the SHE and the Chern insulator state, we plot the current dependence of edge MCD from two points (P1 and P2) at 1.6 K and 6 K (top) and R_{xx} and R_{xy} at 1.6 K (bottom) in Figure 2c. QAH breakdown is observed near 0.5 μA at 1.6 K (the horizontal dashed line marks the resistance quantum). Concurrently, the MCD at P1 switches sign at the QAH breakdown whereas that at P2 increases gradually and saturates. These results suggest that the SHE dominates after the QAH breakdown with increasing bias current.

Figure 3 shows doping dependent non-local spin Hall transport. In this case, we bias the current between two Hall probes to allow for a longer spin propagation channel. The system supports long range spin transport, as evidenced by the MCD images (Figure 3a), MCD line profile (Figure 3b) and the corresponding spin Hall current density (Figure 3c) at varying filling factors (taken at the grey line in Figure 3a). Spin current J_s is normalized to the value at the current path centerline at 3 μm (vertical dashed line). Non-local spin Hall transport and spin accumulation far away from the current path centerline are most significant at lattice filling factor $\nu = 1$ for holes.

Conclusions and Future Steps:

We observe a giant SHE and long-range spin transport in AB-stacked $MoTe_2/WSe_2$ moiré bilayers via MCD imaging. The SHE-induced magnetization nearly saturates spin density under moderate biases. The effect is driven by intrinsic Berry curvature at the Chern insulating state. The effect is the strongest at $\nu = 1$ due to the Berry curvature hot spots and likely a long spin relaxation time, highlighting the potential for spintronics application and advanced quantum devices.

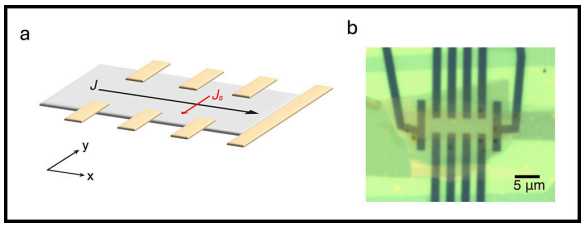

Figure 1: a, Schematic of the spin Hall effect measurements. b, Optical microscope image of a dual-gated device. The scale bar is 5 μm.

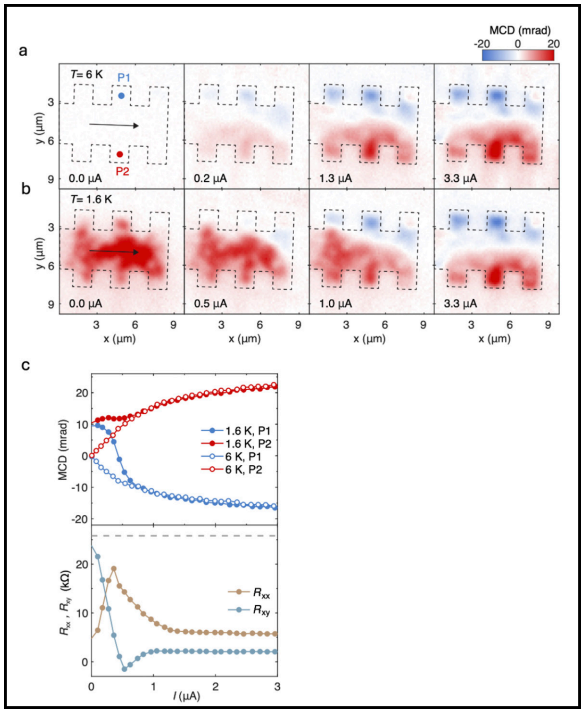

Figure 2: a,b MCD images at varying bias currents at 1.6 K (a) and 6 K (b). c, Bias current dependence of edge spin accumulation and interplay with quantum anomalous Hall breakdown.

References:

[1] Sinova, J., Valenzuela, S. O., Wunderlich, J., Back, C. H., and Jungwirth, T. Spin Hall effects. Rev. Mod. Phys. 87, 1213-1260 (2015).

[2] Kato, Y. K., Myers, R. C., Gossard, A. C., and Awschalom, D. D. Observation of the Spin Hall Effect in Semiconductors. Science 306, 1910-1913 (2004).

[3] Sarma, S. D. Spintronics: Fundamentals and applications. Rev Mod Phys 76, 88 (2004).

[4] Li, T., et al. Quantum anomalous Hall effect from intertwined moiré bands. Nature 600, 641-646 (2021).

[5] Tingxin Li, et al. Continuous Mott transition in semiconductor moiré superlattices. Nature 597, 350-354 (2021).

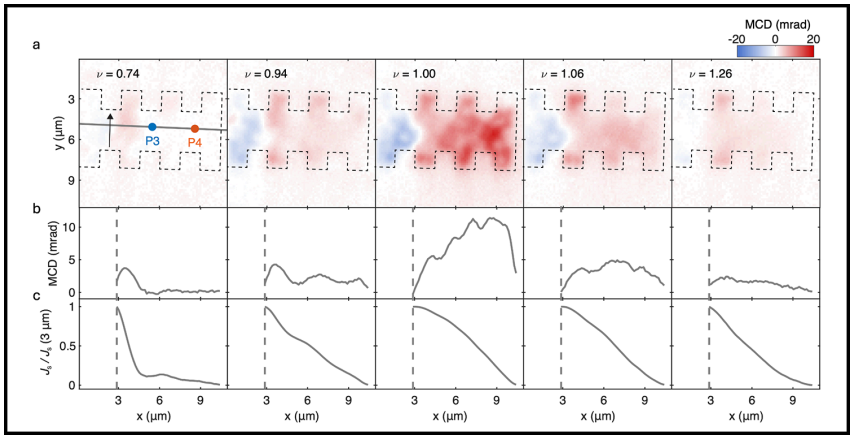

Figure 3: Filling dependence of non-local spin transport. MCD images (a) MCD line profile (b) and the corresponding spin Hall current density (c) at varying filling factors.

Thin-Film Deposition for Surface Characterization Studies for Superconducting Radio Frequency Cavity Application

CNF Project Number: 2779-19
Principal Investigator(s): Matthias Liepe
User(s): Nathan Sitaraman, Sadie Seddon-Stettler

Affiliation(s): Cornell Laboratory for Accelerator-based Sciences and Education, Cornell University

Primary Source(s) of Research Funding: The U.S. National Science Foundation under Award PHY-1549132, the Center for Bright Beams

Contact: mul2@cornell.edu, nss87@cornell.edu, sgs238@cornell.edu

Research Group Website: https://physics.cornell.edu/matthias-liepe

Primary CNF Tools Used: CVC SC4500, AJA Sputter Deposition 1 & 2

Abstract:

Superconducting radio-frequency (SRF) cavities are a key component of particle accelerators (with applications ranging from fundamental physics research to synchrotron X-ray sources, to e-beam microscopy and lithography) and are also being developed for applications in dark matter detection and quantum computing. We are developing next-generation surface treatments to enhance the performance of niobium superconducting surfaces. By using facilities at the CNF, we investigate the effect of metallic doping on the niobium surface. We highlight our recent success in altering the niobium native oxide by zirconium doping and by gold doping.

Summary of Research:

We used CNF's AJA sputter deposition tools to deposit zirconium on niobium sample plates for RF testing. This builds on our earlier development of a zirconium oxide capping layer recipe using the same CNF tool on small coupon samples. Prior to deposition, sample plates received a 60-micron electropolish followed by a 5-hour 800°C vacuum bake and a baseline RF performance test.

The first sample then received an acid wash and high pressure rinsing prior to zirconium deposition at CNF, followed by another 5-hour 800°C vacuum bake. The RF performance of this sample was poor, which post-analysis linked to contamination during transport between CNF and the vacuum furnace.

The second sample similarly received an acid wash and high pressure rinsing, then used a specialized sample holder for clean transport to and from CNF for zirconium deposition. The sample then received an additional high pressure rinse and was delivered to the furnace in the clean-transport holder. This sample will undergo RF testing shortly.

We also used CNF's CVC SC4500 evaporation deposition system to deposit 5-10 nm gold layers on small niobium coupon samples. These samples received short 800°C vacuum bakes, and XPS analysis showed that the resulting surface had greatly reduced niobium oxide concentrations.

Conclusions and Future Steps:

We have now developed two methods to eliminate the niobium pentoxide from a niobium superconducting surface. We expect that this method may be applicable to niobium superconducting devices and niobium-zirconium alloy surfaces, as well as possibly other niobium-based superconducting surfaces which typically form a niobium-rich oxide. We plan to do further RF testing on zirconium-oxide-capped and gold-passivated niobium surfaces in the near future. We will also attempt to apply this method to the Nb_3Sn surface, and we will investigate other passive oxide layers such as hafnium, aluminum, and silicon oxide for SRF applications. We are also using the AJA sputter deposition tool to conduct preliminary investigations of Nb_3Al growth and oxide properties; coupon samples have received aluminum deposition and vacuum baking recipes are currently being finalized for testing.

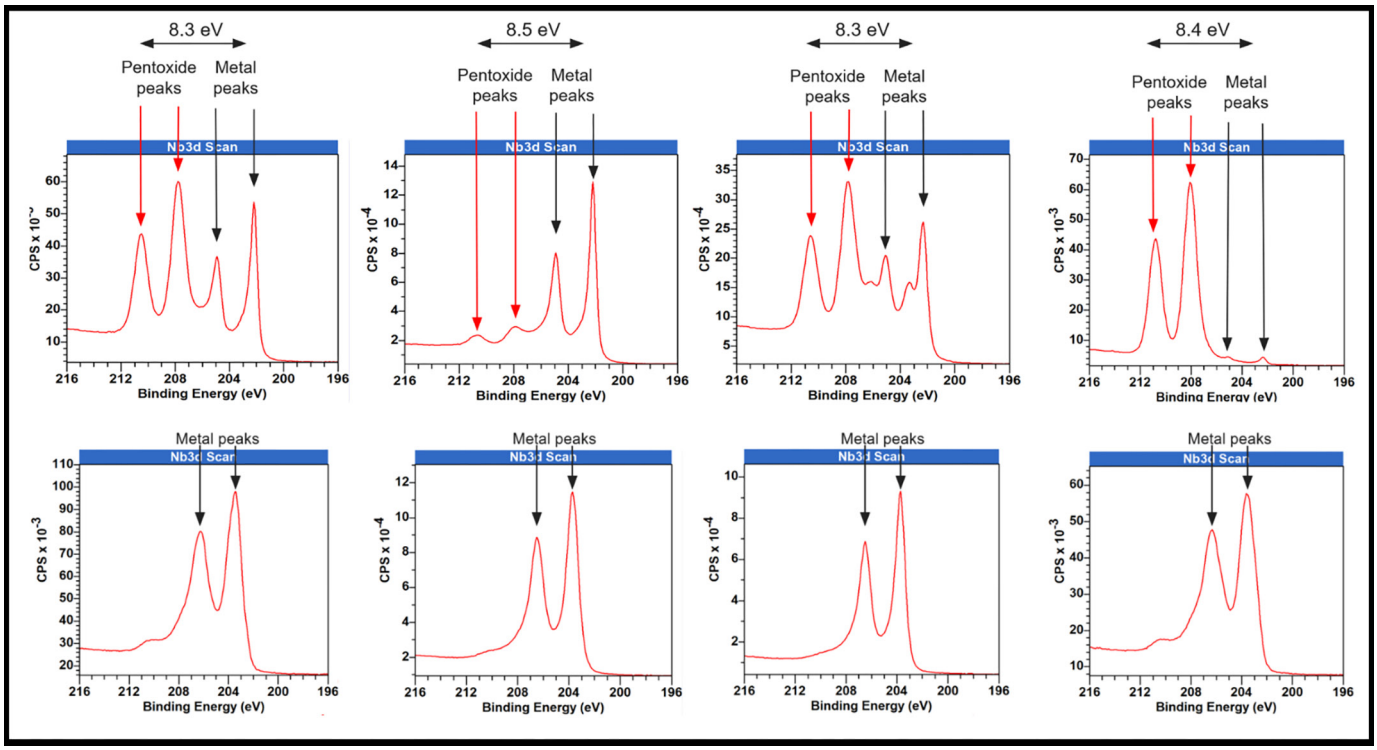

Figure 1: Top row, XPS data from niobium samples of various preparations without gold passivation. Niobium pentoxide peaks are consistently detected at a constant energy shift relative to the niobium metals peaks. Bottom row, XPS data from niobium samples after receiving different gold passivation recipes, none of which have peaks at the expected position for the pentoxide.

References:

[1] Sitaraman, N.S., Sun, Z., Francis, B.L., Hire, A.C., Oseroff, T., Baraissov, Z., Arias, T.A., Hennig, R.G., Liepe, M.U., Muller, D.A. and Transtrum, M.K., 2023. Enhanced Surface Superconductivity of Niobium by Zirconium Doping. Physical Review Applied, 20(1), p.014064.

[2] Seddon-Stettler, S., Liepe, M., Oseroff, T., and Sitaraman, N. Novel materials for beam acceleration. Proc. IPAC'24, 2680-2682.

Imaging Pulse-Induced Charge Density Wave Switching in 1T-TaS_2

CNF Project Number: 2967-21
Principal Investigator(s): Judy J. Cha
User(s): Saif Siddique, Stephen D. Funni, Yu-Mi Wu

Affiliation(s): Department of Materials Science and Engineering, Cornell University

Primary Source(s) of Research Funding: Gordon and Betty Moore foundation (EPiQS Synthesis Award #9062.01), Department of Energy, Basic Energy Sciences DE-SC0023905

Contact: jc476@cornell.edu, ms2895@cornell.edu, sdf68@cornell.edu, yw2658@cornell.edu

Research Group Website: https://cha.mse.cornell.edu

Primary CNF Tools Used: Zeiss Supra SEM, Nabity System for Supra SEM, CHA Evaporator, Harrick Plasma Generator

Abstract:

Charge density wave (CDW) is a macroscopic quantum state observed in low-dimensional materials, such as the two-dimensional (2D) layered material tantalum disulfide (TaS_2). In the 1T polytype of TaS_2, voltage pulses can induce CDW phase transitions, which are accompanied by a sharp insulator-to-metal transition. This makes 1T-TaS_2 promising for next-generation devices. We fabricated nanodevices of 1T-TaS_2 flakes and operated them within a scanning transmission electron microscope (STEM), allowing us to directly visualize the CDW structure and phase transitions during device operation with nanoscale spatial resolution and microsecond temporal resolution at cryogenic temperatures. Our study reveals that Joule heating drives the pulse-induced CDW transitions and the CDW transitions are directly correlated with the real-space structure and electronic properties of the material, which is crucial for developing reliable and scalable TaS_2-based electronics.

Summary of Research:

Charge density waves (CDWs) are periodic modulations of the electronic charge density within a material, which are accompanied by periodic distortions in the material's crystal lattice [1]. 1T-TaS_2 is a 2D quantum material that hosts several distinct CDW phases [2]. These include an insulating commensurate (C) CDW phase with long-range order, a metallic nearly-commensurate (NC) phase characterized by domains of commensurate CDW separated by phase slips (discommensurations), and a metallic incommensurate (IC) CDW phase lacking long-range order [3]. Below 200 K, 1T-TaS_2 is in the insulating C-CDW phase, but voltage pulses can switch it to the metallic NC-CDW phase [4]. This switching is fast, reversible and energy efficient, and results in a large change in electrical resistance, making 1T-TaS_2 promising for use in memristive and neuromorphic devices [5]. However, the mechanism of pulse-induced switching is not fully understood. To use TaS_2 in nanoscale devices, it is crucial to have a detailed understanding of how the CDW phase transitions occur at nanoscale dimensions, and what factors affect the transition.

We fabricated 2-terminal devices by exfoliating ~ 55 nm thick flakes of 1T-TaS_2 from bulk crystals onto *in-situ* TEM chips. Electrical connections to the platinum electrodes on the *in-situ* TEM chips were made by placing graphite electrodes on the TaS_2 flakes (Figure 1a,b). We operated this device within a TEM using a Keithley 2400 source meter to measure the resistance of the flake as a function of temperature. Simultaneously, electron diffraction was acquired to measure the domain size (D_{NC}), the order parameter for the C to NC transition in 1T-TaS_2, hence characterizing its CDW state (Figure 1c) [6]. In the C-CDW phase, D_{NC} is > 100 nm while in the NC-CDW phase, D_{NC} is ~ 10 nm (Figure 1).

By applying a constant DC bias and heating the flake from the C to NC phase, we monitored the device resistance and D_{NC} (Figure 1c,d). We found that the domain size changes first, followed by the resistance change, showing that the structural CDW transition precedes the resistive transition by about 10 K, as indicated by changes in resistance and domain size during the C to NC transition (inset Figure 1d). This is unexpected, as the structural and electronic changes due to CDW transitions are assumed simultaneous.

To investigate this further, we applied a series of short square pulses with increasing voltage amplitudes (2 V to 9.6 V, 3 μs pulse duration; Figure 2) to the TaS_2 flake in its C-CDW phase, using a Keysight 33600A waveform generator. For voltage pulses > 3.2 V, the flake transitions to the NC phase (Figure 2). Consistent with our earlier findings the structural CDW transition

preceded the electronic resistance transition. Additionally, larger voltage pulses produced smaller CDW domains and lower device resistance in the NC phase, suggesting that the applied voltage increases the temperature of the device through Joule heating.

To demonstrate that Joule heating drives the switching, we applied triangular voltage ramps (with maximum voltage between 0.1 V to 1.2 V) while collecting diffraction patterns at every 10 ms interval. We observed that voltages above 0.8 V caused a sudden decrease in DNC, indicating a transition from the C to NC and IC phases (Figure 3a). We extracted the in-plane flake strain from the diffraction data and converted it to corresponding temperature using thermal expansion coefficient.

At the 0.8 V threshold, we measure the flake temperature to be ~200 K, which corresponds to the C to NC transition temperature (Figure 3b). Thus, Joule heating from the applied voltage is sufficient to raise the temperature of 1T-TaS_2 devices above the CDW transition temperature.

Conclusions and Future Steps:

Our study conclusively demonstrates that bias-induced switching in 1T-TaS_2 is driven by Joule heating, causing a rapid thermal transition from the C to NC and IC phases. This mechanism applies for both steady-state biasing and microsecond voltage pulses. Further work is needed to study the claims of picosecond switching with energies below the Joule heating threshold, to determine if purely field-induced switching is possible. Our findings provide a microscopic understanding of CDW behavior in TaS_2 devices and provide a foundation for future studies to enhance the performance and reliability of TaS_2-based electronic devices.

References:

[1] Grüner, Rev. Mod. Phys. 60, 1129 (1988).

[2] Ishiguro and Sato, Phys. Rev. B 44, 2049 (1991).

[3] Lee, et al., Phys. Rev. Lett., 122, 106404 (2019).

[4] Hollander, et al., Nano Lett. 15, 1861-1866 (2015).

[5] Mihailovic, et al., Appl. Phys. Lett. 119, 013106 (2021).

[6] Hart, et al., Nat. Commun. 14, 8202 (2023).

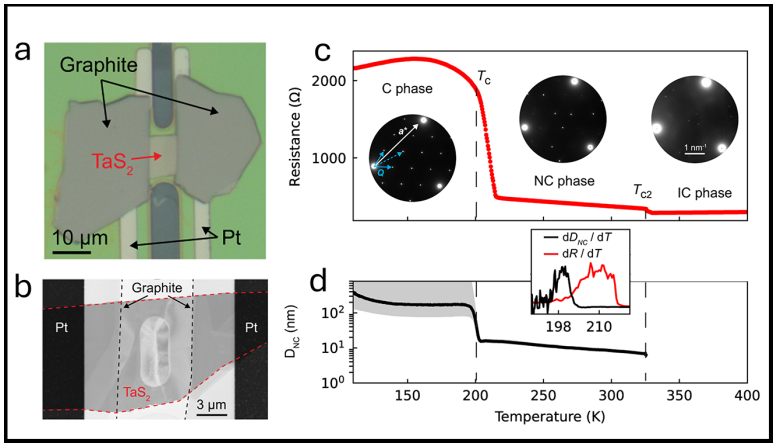

Figure 1: a. Optical microscope image of the studied device. b. STEM image of the same device. c. Resistance vs. temperature of the TaS_2 device measured in-situ *inside the TEM. Insets show associated electron diffraction pattern for each phase. d. Doman size (D_{NC}) as a function of temperature. The inset shows the temperature derivatives of the resistance and D_{NC}.*

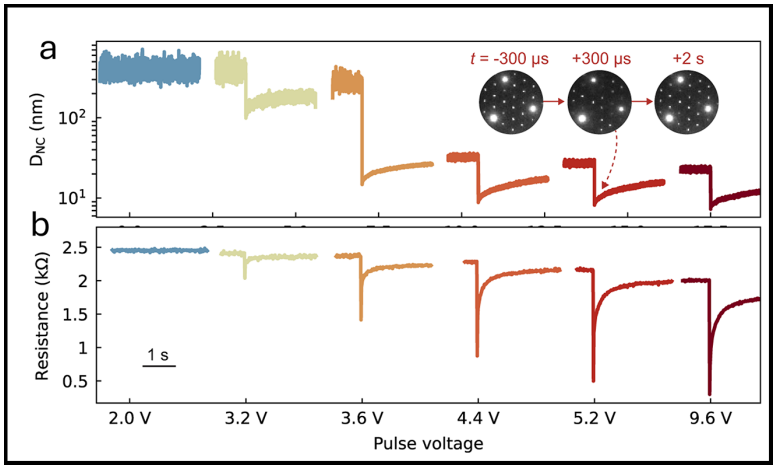

Figure 2: a. Time-resolved CDW domain size D_{NC}, and b. device resistance during pulsing.

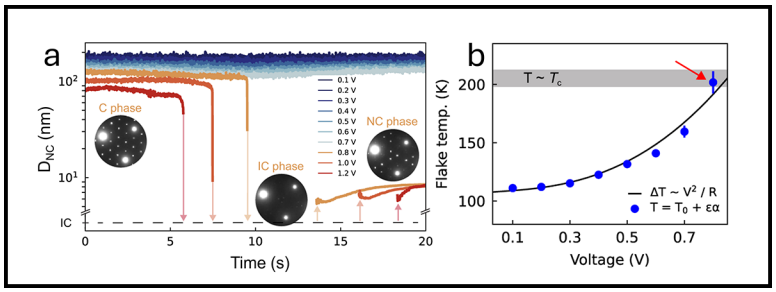

Figure 3: a. Measured D_{NC} during voltage ramps, with maximum voltage ranging from 0.1 V to 1.2 V. Insets show the diffraction pattern snapshots acquired during the 0.8 V ramp. b. Maximum flake temperature for voltage ramps from 0.1 V to 0.8 V.

Manufacturing SiN Bullseye Cavities and SOI Photonic Crystal Nanobeam Cavities

CNF Project Number: 3008-22
Principal Investigator(s): Professor Pablo A. Postigo
User(s): Christopher (Christer) Everly, Martin Sanchez

Affiliation(s): Institute of Optics, University of Rochester

Primary Source(s) of Research Funding: UoR Startup URA Award 2023-2024 from University of Rochester

Contact: ppostigo@ur.rochester.edu, ceverly@ur.rochester.edu, msanch23@ur.rochester.edu

Research Group Website: https://www.postigolab.com

Primary CNF Tools Used: JEOL 6300 & 9500, E-beam Spin Coaters, Olympus MX-50 Microscopes, Oxford 82, Oxford 100, PT770 RIE, Oxford Cobra ICP, Plasma-Therm Tikachi HDP-CVD, Oxford PECVD, Primaxx Vapor HF Etcher, Yes EcoClean Asher, Yes Asher, Filmetrics systems, Zeiss Ultra SEM, Zeiss SEM Supra, Veeco AFM, DISCO Dicer Saw

Abstract:

Our group is interested in quantum research on photonic platforms. Some topics we are currently exploring include: on-chip lasing and single-photon emission enhancement with circular Bragg gratings, and room temperature single phonon quantum sensing using phononic crystal enhanced optomechanical cavities. There have been recent reports of Purcell enhancement from circular Bragg cavities, as well as mechanical ground states being achieved at room temperature through use of well-designed phononic crystals.

Summary of Research:

Users have done diligent work to refine the fabrication process for the circular Bragg grating (CBG) cavity, colloquially referred to as a bullseye cavity. A deposition recipe was developed on the Oxford PECVD that achieves repeatable SiO_2 followed by SiN deposition thicknesses. Experimentation was completed on different gas pressures during inductively coupled plasma (ICP) etching of silicon nitride in order to achieve the high aspect ratio, anisotropic etches required for the silicon nitride (SiN) bullseye cavities.

Additionally, the group has created our first fabrication procedure for creating suspended structures like nanobeams and phononic crystals. Due to the fine transverse structures required to make photonic crystal cavities, experimentation has been done with e-beam resist type, thickness, and dosage applied in lithography machines to match designed requirements. Experimentation was also completed on applying a varied bias to different regions in pattern files in order to account for reactive ion etch lag (RIE lag) affecting the transverse dimensions of nanostructures differently than larger structures. Different chemistries have been attempted in the lab to create anisotropic silicon etches during pattern transfer with great successes being achieved with a hydrobromic acid (HBr) inductively coupled plasma (ICP) etch, instead of the sulfur hexafluoride and oxygen (SF_6/O_2) chemistry frequently seen in literature for silicon etches. Finally, experimentation was completed with vapor hydrogen fluoride (HF) etching to successfully create suspended structures without any stiction. This was successful for suspended features in the tested range of tens of microns.

Conclusions and Future Steps:

Correcting the critical dimension blur is the last step to successful bullseye fabrication. After that is verified the next steps for the bullseye cavities will be to optically characterize the cavity resonance in lab.

As the nanobeam and phononic crystal fabrication is still in its incipiency, many next steps need to be taken both in the lab at University of Rochester and in the lab at Cornell. The fabricated nanobeams also need to be optically characterized. Many nanobeams were created with varying biases and cavity lengths with the hopes of pin-pointing an optical resonance in a new optical setup at the University of Rochester. Experiments need to be done with the HF vapor etch of much larger suspended structures. Simulations indicate that more phononic crystal layers increase mechanical *Q*-factor, so experiments need to be completed to make sure large, suspended structures in the range of hundreds of microns can be fabricated successfully using the same HF vapor etch without issues of stiction. Great success was achieved with the anisotropic HBr pattern transfer etch. More experiments need to be completed on the replicability of these results.

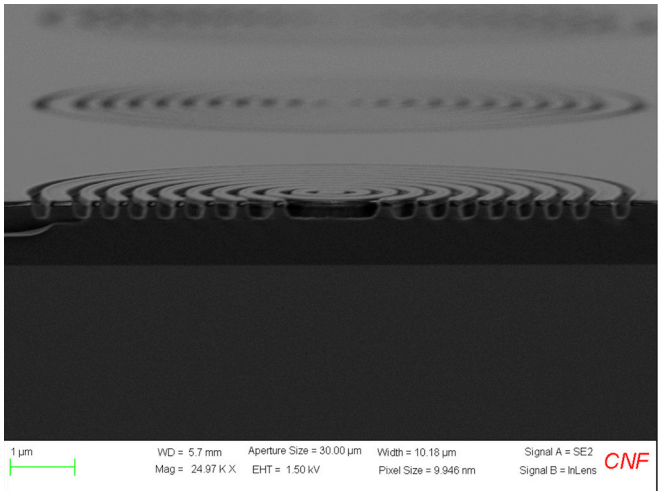

Figure 1: Cross-section of a bullseye cavity.

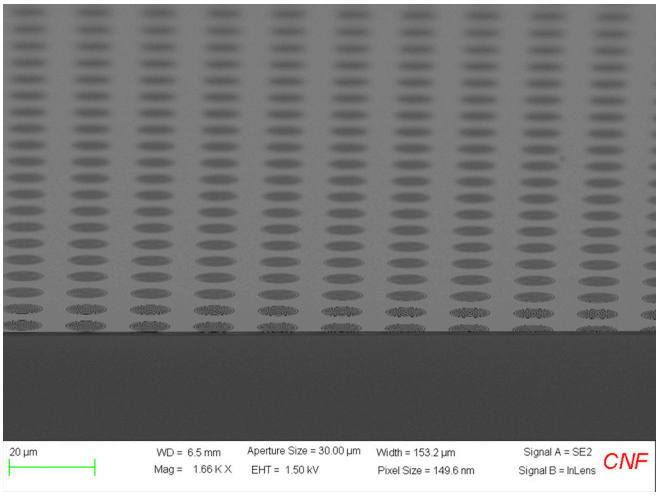

Figure 2: Array of bullseye cavities.

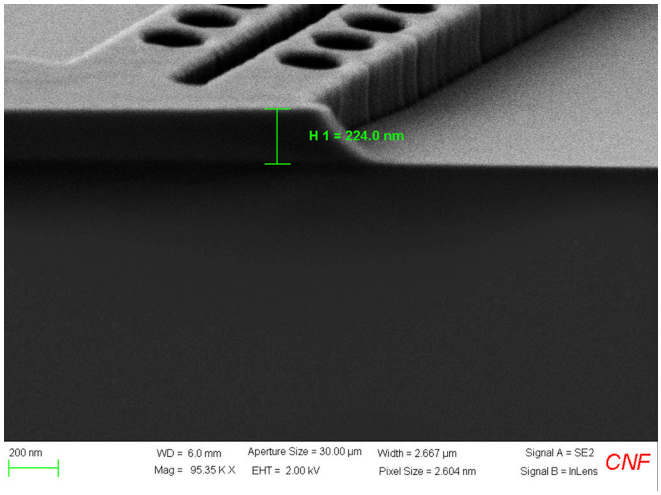

Figure 3: Cross section of nanobeams before release showing the device layer and pattern still with resist taken with the Zeiss SEM Ultra.

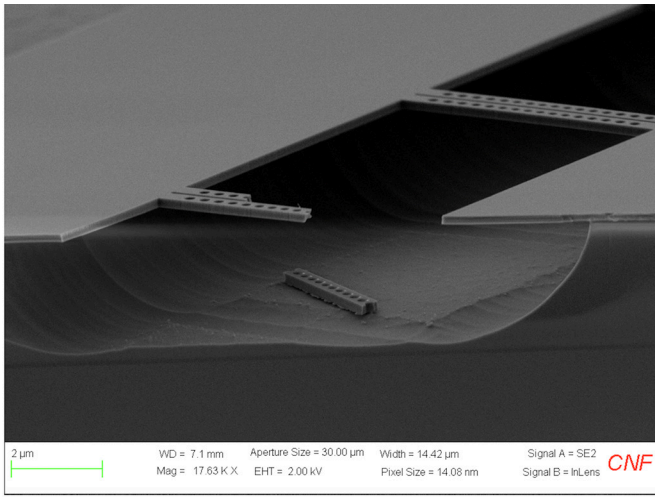

Figure 4: Nanobeam intentionally broken to show fully etched photonic crystal holes with intact suspended nanobeams in the background, taken with the Zeiss SEM Ultra.

References:

[1] "Room-Temperature Lasing in Colloidal Nanoplatelets via Mie-Resonant Bound States in the Continuum"; Mengfei Wu, Son Tung Ha, Sushant Shendre, Emek G. Durmusoglu, Weon-Kyu Koh, Diego R. Abujetas, José A. Sánchez-Gil, Ramón Paniagua-Domínguez, Hilmi Volkan Demir, and Arseniy I. Kuznetsov, Nano Letters 2020 20 (8), 6005-6011, DOI: 10.1021/acs.nanolett.0c01975.

[2] "Enhanced Emission from WSe_2 Monolayers Coupled to Circular Bragg Gratings"; Ngoc My Hanh Duong, Zai-Quan Xu, Mehran Kianinia, Rongbin Su, Zhuojun Liu, Sejeong Kim, Carlo Bradac, Toan Trong Tran, Yi Wan, Lain-Jong Li, Alexander Solntsev, Jin Liu, and Igor Aharonovich ACS Photonics 2018, 3950-3955 DOI: 10.1021/acsphotonics.8b00865.

[3] "Exploring Regenerative Coupling in Phononic Crystals for Room Temperature Quantum Optomechanics"; Lukas M. Weituschat, Irene Castro, Irene Colomar, Christer Everly, Pablo A. Postigo, and Daniel Ramos, Scientific Reports 14, Article number: 12330 (2024), DOI: https://doi.org/10.1038/s41598-024-63199-1.

[4] "Resolved-sideband cooling of a micromechanical oscillator"; A. Schliesser, R. Rivière, G. Anetsberger, O. Arcizet, and T.J. Kippenberg Nature Physics 4, 415-419 (2008), DOI: 10.1038/nphys939.

Weak Link Superconducting Quantum Interference Devices for High-Resolution Scanning Magnetometry

CNF Project Number: 3017-22
Principal Investigator(s): Katja Nowack
User(s): Alex Striff

Affiliation(s): Laboratory of Atomic and Solid State Physics, Cornell University

Primary Source(s) of Research Funding: Air Force Office of Scientific Research (Muri FY21 Tunneling Phenomena in Interface Superconductors)

Contact: kcn34@cornell.edu, abs299@cornell.edu

Research Group Website: https://nowack.lassp.cornell.edu

Primary CNF Tools Used: AJA Sputter Deposition Tool (I), JEOL JBX-6300FS 100 kV Electron Beam Lithography System, CVC SC4500 Combination Thermal/E-gun Evaporation System (Odd-hour), Angstrom Load Lock E-beam Evaporator, DWL2000 Laser Pattern Generator and Direct Write System, Oxford PlasmaLab 80+ RIE System (Oxford 81), Zeiss Ultra 55 Scanning Electron Microscope

Abstract:

Magnetic imaging is a powerful tool for studying quantum materials. To make a sensitive magnetometer for use in a scanning probe microscope, a small super-conducting loop is interrupted by two Josephson junctions to create a super-conducting quantum interference device, or SQUID, which converts the magnetic flux coupled into the loop into a measurable signal. This research explores one way to increase the spatial resolution and maximum operating field of a SQUID, which is to replace the often-used superconductor-insulator-superconductor (SIS) Josephson junctions with narrow constrictions (weak links) in the super-conducting loop, which allow the size of the loop to be less than 1 μm [1]. Initial measurements have demonstrated the sensitivity of test SQUIDs to magnetic flux, with improvements in progress.

Summary of Research:

Figure 1 depicts a weak link SQUID, made of a 50 nm niobium film with a 20 nm aluminum shunting layer on a silicon substrate. For the weak links to behave like Josephson junctions, they must have dimensions comparable to the super-conductor's coherence length [2], which necessitates the use of electron beam lithography to pattern a mask for the SQUID loop. A bilayer lift-off process patterns the SQUID loop in 20 nm of aluminum. Since the electron beam write time for bond pads would be excessive, instead a separate 20 nm layer of aluminum that overlaps with the SQUID loop is patterned by direct-write photolithography and lifted off. The two aluminum layers mask the niobium during a dry etch step, leaving a bilayer SQUID pattern with the layer stack depicted in Figure 2.

A SQUID with slightly different dimensions to those depicted in Figure 1 was measured in a liquid helium dipping probe setup at 4.6 K. As is the case for conventional SIS junction SQUIDs, a series SQUID array amplifier was used to voltage bias and read out the weak link SQUID, which avoids issues encountered when using noisy, high-impedance room temperature amplifier electronics [3]. Figure 3 depicts the voltage output from the array as a function of the magnet current applying a magnetic flux to the SQUID. The array output voltage modulates with flux, demonstrating that the niobium constrictions are behaving like weak links, as intended.

Conclusions and Future Steps:

While these weak link SQUIDs operate as magnetic flux sensors, some aspects of their behavior and use in a readout circuit are not fully understood. Future work will continue to explore the design parameter space for these devices. We will also develop an etching process to place the SQUID loop at the corner of a chip so that it may scan across a sample surface [4].

References:

[1] Vasyukov, D., et al. Nature Nanotech 8, 639-644 (2013).

[2] Likharev, K. K. Rev. Mod. Phys. 51, 101-159 (1979).

[3] Huber, M. E., et al. Review of Scientific Instruments 79, 053704 (2008).

[4] Pan, Y. P., et al. Supercond. Sci. Technol. 34, 115011 (2021).

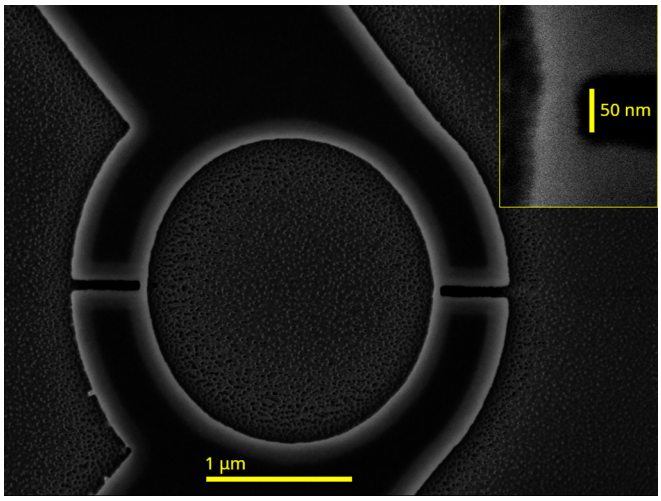

Figure 1: Scanning electron microscope image of the SQUID loop. Inset: Right constriction at higher magnification.

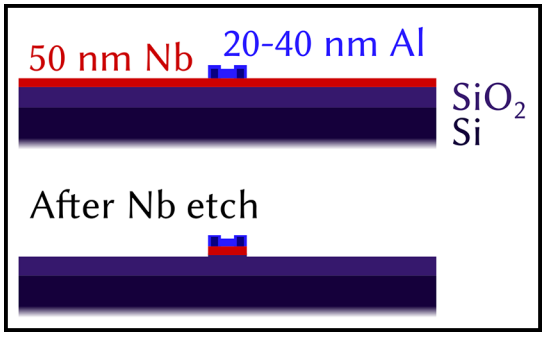

Figure 2: The SQUID fabrication process patterns a niobium film on a silicon substrate by using an aluminum hard mask (made of two overlapping aluminum layers to reduce the write time for electron beam lithography). A dry etch process transfers the aluminum pattern into the niobium.

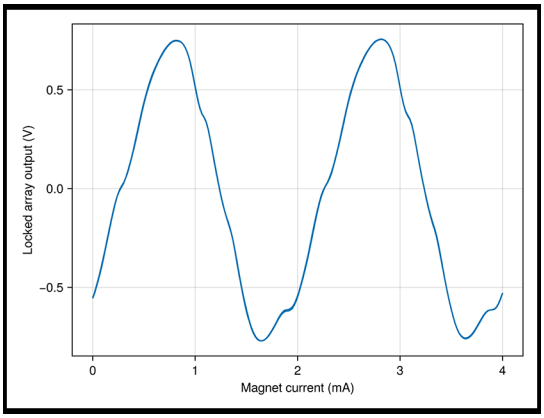

Figure 3: The voltage output of a series SQUID array amplifier (operated in a flux feedback locked loop) oscillates in response to a magnet coupling magnetic flux into a SQUID loop similar to the loop in Figure 1. Refinements to this readout scheme are in progress.

Fabrication of Fluxonium-Like Qubits

CNF Project Number: 3067-23
Principal Investigator(s): Ivan Pechenezhskiy
User(s): Benjamin Byrd, Kesavan Manivannan

Affiliation(s): Department of Physics, Syracuse University

Primary Source(s) of Research Funding: Syracuse University, Army Research Office

Contact: ivpechen@syr.edu, babyrd@syr.edu, kmanivan@syr.edu

Primary CNF Tools Used: ASML DUV Stepper, JEOL 6300, PT770 Plasma Etcher, Oxford81 Etcher, Heidelberg DWL2000 Mask Writer

Abstract:

We fabricate fluxonium and fluxonium-like qubits to study their potential for quantum computations, with our most recent study being focused on the behavior of broken Cooper pairs (quasiparticles) in superconducting coherent quantum devices. Quasiparticles are injected directly into our samples by driving a current through a Josephson junction larger than its critical current. Fluxonium qubits are intrinsically protected against charge noise and also against flux noise at the two flux sweet spots, making it easier to produce longer-lived devices. Some of these qubits have lifetimes exceeding a millisecond [1].

This project's fluxonium-like qubits are fabricated following a previously reported recipe [2].

Summary of Research:

A fluxonium qubit (Figure 1) is composed of a capacitor, with a Josephson junction shunting the capacitive element. The key difference between a fluxonium and the more commonly studied transmon qubit is the inclusion of an inductor made of a chain of Josephson junctions, which shunts the two capacitor pads (Figure 2). This forms a closed loop through which we can apply a magnetic field. At certain values of flux threading through this loop, the qubit is protected from some crucial loss channels. The qubit is capacitively coupled to a resonator, whose frequency is shifted based on the state of the fluxonium qubit, allowing us to determine the state of the qubit by measuring the shift in the resonator frequency.

Our devices are fabricated on Si wafers, first by sputtering a ~ 70 nm layer of niobium to act as a superconducting ground plane from which we pattern microwave resonators, capacitors and co-planar waveguides. After patterning large features using the ASML DUV stepper for photolithography, the pattern is etched into the niobium using the PT770. After this, the devices are cleaned in the CNF hot strip bath, the Glen1000, then in a bath of 10:1 DI:HF. To form Josephson junctions, which are of the order of ~ 100 nm × 100 nm, e-beam lithography using the JEOL 6300 is required. After the junction is patterned in the JEOL 6300, the junctions are formed via e-beam evaporation using the Dolan bridge technique at Syracuse University.

By fabricating samples with a wide range of different geometries, we have been able to tune our fabrication process to improve coherence times in our devices by an order of magnitude. Additionally, adjusting the geometry of our Al/AlOx/Al Josephson junctions in the array enables us to tune the phase-slip rate across each junction, improving dephasing times for these devices as well [3]. In the near future we expect that these changes will improve our qubit dephasing times by an order of magnitude as well.

Extending our fabrication repertoire further, we have also begun to work on the Xactix XeF_2 etcher. With this, we will be able to suspend all Josephson junctions similar to the junctions in the blochnium qubit [4], giving us a wider range of accessible qubit parameters and new avenues to probe qubit dynamics.

References:

[1] A. Somoroff, et al. Millisecond Coherence in a Superconducting Qubit. Phys. Rev. Lett. 130, 267001 (2023). https://doi.org/10.1103/PhysRevLett.130.267001.

[2] V. Iaia, et al. Phonon downconversion to suppress correlated errors in superconducting qubits. Nature Communications 13, 6425 (2022). https://doi.org/10.1038/s41467-022-33997-0.

[3] M. Randeria, et al. Dephasing in Fluxonium qubits from Coherent Quantum Phase Slips. arXiv:2404.02989.

[4] I. V. Pechenezhskiy, et al. The superconducting quasicharge qubit. Nature 585, 368 (2020). https://doi.org/10.1038/s41586-020-2687-9.

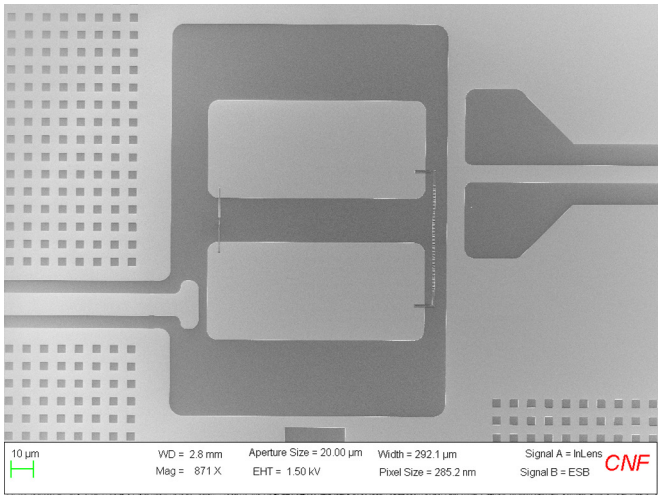

Figure 1: Scanning electron microscopy (SEM) image of one of the fluxonium qubits taken at CNF.

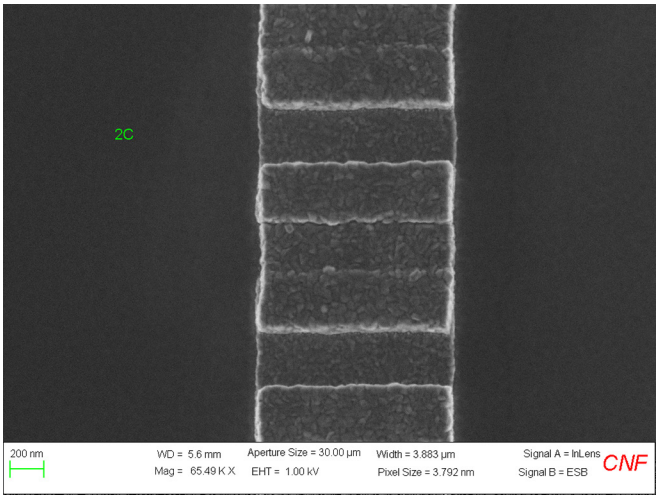

Figure 2: SEM image of a Josephson junction chain, taken at CNF.

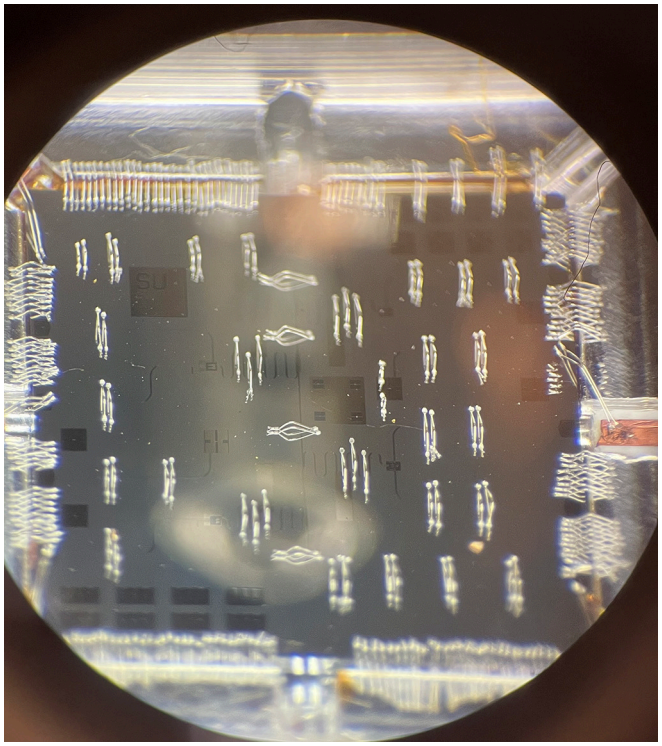

Figure 3: Photograph of a sample set into the holder wire-bonded for low-temperature measurements.

Characterization of Fluxonium Qubits

CNF Project Number: 3067-23
Principal Investigator(s): Ivan Pechenezhskiy
User(s): Benjamin Byrd, Kesavan Manivannan

Affiliation(s): Physics Department, Syracuse University

Primary Source(s) of Research Funding: Army Research Office

Contact: ivpechen@syr.edu, babyrd@syr.edu, kmanivan@syr.edu

Primary CNF Tools Used: ASML DUV Stepper, JEOL 6300, PT770 Plasma Etcher, Heidelberg DWL2000 Mask Writer

Abstract:

We fabricate and characterize superconducting fluxonium qubits, which are among the leading qubit candidates for scalable quantum computing processors. They possess very high (millisecond-long) characteristic times and large anharmonicity [1]. A comprehensive characterization of the different noise channels that affect fluxonia is required to devise appropriate mitigation strategies to enhance qubit performance for fault-tolerant operation. We aim to study the different extrinsic and intrinsic decoherence mechanisms that affect this qubit. In particular, we perform experiments to understand the quasiparticle effects in fluxonia.

Summary of Research:

Superconducting quantum systems have emerged as one of the leading platforms for quantum computing. Josephson tunnel junctions are the backbone of these superconducting qubits, providing the required anharmonicity. A fluxonium qubit consists of a small Josephson junction connected to two large capacitor pads and a chain of Josephson junctions acting as a large inductor [2].

An external magnetic flux is applied to tune the properties of this qubit. At the sweet spot, when a half-integer superconducting flux quantum threads the loop, the qubit exhibits a very high coherence, large anharmonicity, and is protected from flux noise decoherence.

The SEM image of our fluxonium qubit fabricated at CNF is shown in Figure 1a. The two niobium capacitor pads (40 μm × 80 μm each) set the capacitive energy scale $E_C/h \sim 1.31$ GHz. The Al/AlOx/Al small Josephson junction (90 nm × 100 nm) between the pads determines the Josephson energy $E_J/h \sim 1.29$ GHz. The array of 130 Josephson junctions (1.3 μm × 0.1 μm each) to the immediate right of the pads is associated with the inductive energy $E_L/h \sim 0.21$ GHz. In the multistep fabrication process, we utilized photolithography and electron-beam lithography tools at CNF, and an electron-beam evaporator and sputtering system at Syracuse University. The flux bias line can be seen in the right part of Figure 1a. Each qubit is capacitively coupled to a coplanar waveguide resonator, shown in the left part of Figure 1a, for dispersive readout of the qubit state. Figure 1b displays the injector Josephson junction, which can be brought to its resistive state to inject pair-breaking phonons and create quasiparticles at the qubit junctions [3].

The fabricated qubit is housed inside a sample box that sits on the 10 mK plate of a dilution refrigerator. Using the injector junction, we control the quasiparticle environment of the qubit to distinguish quasiparticle-induced effects from other decoherence channels. Figure 2 shows the exponential decay curves of the qubit T_1 measurement with (orange) and without (blue) a quasiparticle injection pulse. Compared to the baseline, we observe degradation in qubit energy relaxation time when the quasiparticle density at the qubit is elevated. Figure 3 shows the qubit T_1 as a function of external flux in three different situations: without injection, 2 μs injection, and 4 μs injection, illustrating a reduction in T_1 with injection. In the near future, we plan to study the effect of design variations in device geometry on inferred quasiparticle densities in the small and array junctions of fluxonia.

References:

[1] A. Somoroff, et al. Phys. Rev. Lett. 130, 267001 (2023). https://doi.org/10.1103/PhysRevLett.130.267001.

[2] L. Nguyen, et al. Phys. Rev. X 9, 041041 (2019). https://doi.org/10.1103/PhysRevX.9.041041.

[3] V. Iaia, et al. Nature Communications, 13, 6425 (2022). https://doi.org10.1038/s41467-022-33997-0.

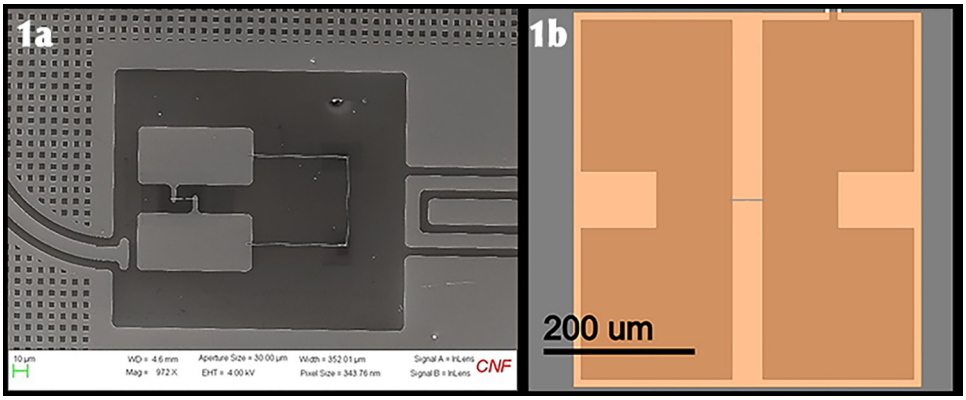

Figure 1: (a) SEM image of the fluxonium qubit showing the capacitor pads, single Josephson junction, and the chain of Josephson junctions. (b) Injector Josephson junction.

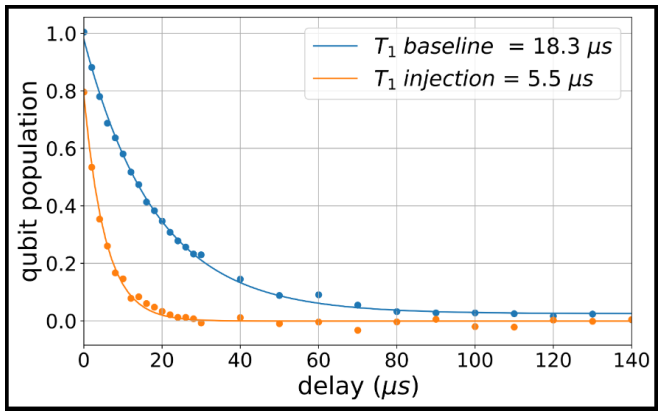

Figure 2: T_1 traces measured at $\Phi_{ext} = 0.0\ \Phi_0$ for the baseline and injection cases.

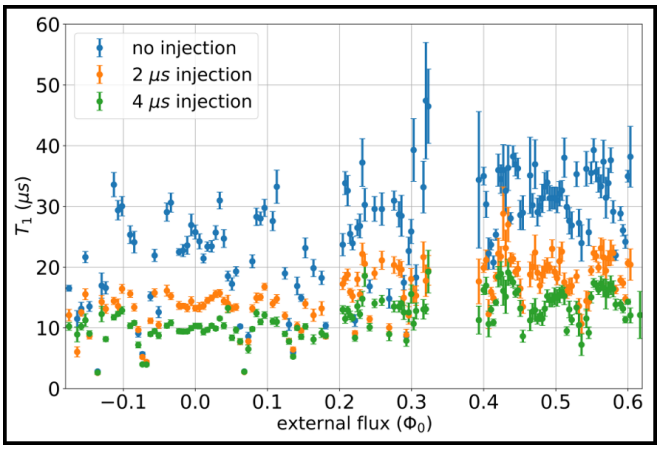

Figure 3: T_1 versus external flux for a fluxonium qubit measured in three cases: baseline, with 2 μs injection pulse length, and with 4 μs injection pulse length.

Probing Two-Dimensional Van der Waal Heterostructure and Height Characterization

CNF Project Number: 3098-23
Principal Investigator(s): Pankaj K. Jha
User(s): Jagi Rout

Affiliation(s): Department of Electrical Engineering and Computer Science (EECS), Syracuse University

Primary Source(s) of Research Funding: Syracuse University EECS Startup Funds

Contact: pkjha@syr.edu, jarout@syr.edu

Research Group Website: https://qutechlab.syr.edu/

Primary CNF Tools Used: Heidelberg Mask Writer - DWL2000, AFM Veeco Icon, DWL2000, Angstrom Evaporator, Odd and Even Hour Evaporator

Abstract:

This study describes a method for creating metal probes on Si/SiO_2 substrates. These probes are important for making measurements on superconducting 2D flakes in order to understand the transport properties of our superconductor and determine the critical current specific to our material. The fabrication process involves depositing metal layers precisely using techniques such as photolithography and electron beam evaporation. We optimized key parameters including substrate preparation, metal deposition rates, and patterning resolution to produce high-quality metal probes with excellent electrical and mechanical properties. The resulting metal probes show superior conductivity, durability, and adhesion to the Si/SiO_2 substrates. This work shows that the proposed fabrication method is feasible and scalable, offering potential for developing high-performance devices in microelectronics and nanotechnology.

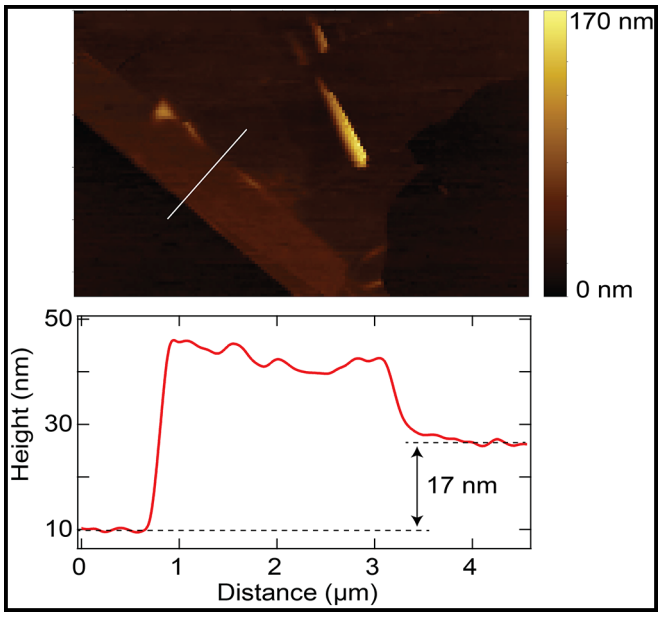

Figure 1: AFM study gives a thickness of 17.0 nm which corresponds to .28 layers [4].

Summary of Research:

Atomic Force Microscopy (AFM) is a widely used technique for measuring the thickness of two-dimensional (2D) materials down to a monolayer. Materials like graphene, molybdenum disulfide (MoS_2), and hexagonal boron nitride (hBN) have unique electronic, optical, and mechanical properties that depend largely on their thickness. Accurate determination of material thickness is essential for understanding and utilizing these properties in various applications, including electronics, photonics, and sensing. In AFM, a sharp tip attached to a cantilever scan over the sample surface. As the tip interacts with the sample, forces between the tip and the sample cause the cantilever to deflect. These deflections are measured by a laser beam reflected off the cantilever onto a photodetector. By maintaining a constant force (contact mode) or distance (tapping mode) between the tip and the sample, AFM can generate high-resolution topographic images of the sample surface.

The sample needs to be meticulously prepared in order to measure the thickness of 2D material flakes using AFM. This process usually entails separating the 2D material from a larger crystal onto a substrate, commonly silicon with a silicon dioxide (Si/SiO_2) layer. The flatness and cleanliness of the substrate are crucial for precise measurements.

After preparing the sample, we use AFM to scan the surface and generate a topographic image. We can then

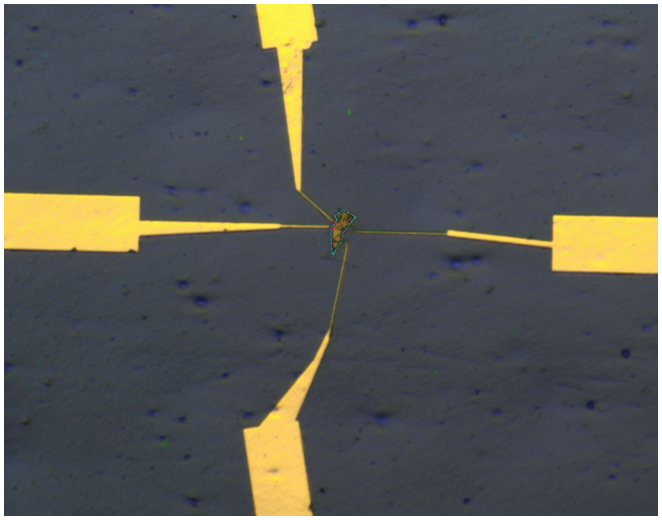

Figure 2: Ti/ Au contacts fabricated to probe superconducting flake Fe(Te,Se).

analyze the height profile of the image to determine the thickness of the 2D material flakes. The thickness is measured by comparing the height difference between the flake and the surrounding substrate. To ensure accurate measurements, it's important to select an area of the substrate adjacent to the flake as a reference point.

The critical current defines the operational limits of superconducting devices [4]. For applications in quantum computing and nanoelectronics, it is crucial to know the maximum current that the superconductor can handle without becoming resistive. Higher critical currents enable the development of more powerful and efficient superconducting circuits and devices.

Superconductors with higher transition temperatures can operate at more practical and potentially higher temperatures. This reduces the need for expensive cooling systems, which is especially important for developing superconducting electronics that can function at or near room temperature. This greatly enhances their practicality and cost-effectiveness.

By probing the critical current, researchers can identify the factors that limit superconducting performance. This knowledge can be used to engineer materials with higher critical currents through strain engineering, doping, or creating heterostructures [3]. We used DWL66FS to write directly on Si/SiO_2 substrates, followed by metal deposition in the Angstrom evaporator. Ti/Au – 5/95 nm was deposited on the developed substrates exposed in DWL2000. Different feature sizes were experimented with while doing the direct writing, and a dose test was performed to optimize the energy required in the exposure. The bilayer photoresist spin coating option was preferred for the direct writing to minimize the undercut for the metal lift-off with acetone. Optimizing Ic can lead to the development of superior superconducting materials with tailored properties for specific applications [1,2].

Understanding the factors that influence the critical temperature (T_c) in 2D superconductors is important, as this understanding can help in the synthesis of new materials with higher transition temperatures. This may involve exploring new material systems, such as transition metal dichalcogenides (TMDs) or other layered compounds and manipulating their structure at the atomic level to enhance their superconducting properties [4].

We will work on etching our material to create nanostrips and study its electrical and optical properties.

References:

[1] Qiu, G., Yang, HY., Hu, L., et al. Emergent ferromagnetism with superconductivity in Fe(Te,Se) van der Waals Josephson junctions. Nat Commun 14, 6691 (2023).

[2] Qiu, Gang, et al. "Concurrent Ferromagnetism and Superconductivity in Fe(Te,Se) van der Waals Josephson Junctions." arXiv preprint arXiv:2303.00966 (2023).

[3] Lee J, Lee W, Kim GY, Choi YB, Park J, Jang S, Gu G, Choi SY, Cho GY, Lee GH, Lee HJ. Twisted van der Waals Josephson Junction Based on a High-Tc Superconductor. Nano Lett. 2021 Dec 22;21(24):10469-10477.

[4] A. K. Pattanayak, et al. Temperature-Dependent Optical Constants of Nanometer-thin Flakes of Fe(Te,Se) Superconductor in the Visible and Near-Infrared Regime (Manuscript under communication).

Observation of Exciton Polariton Band Structure

CNF Project Number: 3114-23
Principal Investigator(s): Bo Zhen
User(s): Zhi Wang

Affiliation(s): Department of Physics and Astronomy, University of Pennsylvania

Primary Source(s) of Research Funding: DARPA, ONR, Sloan foundation

Contact: bozhen@sas.upenn.edu, zhiw@sas.upenn.edu

Research Group Website: https://web.sas.upenn.edu/bozhen/

Primary CNF Tools Used: Plasma Enhanced Chemical Vapor Deposition (PECVD), Chemical Mechanical Polishing

Abstract:

Exciton polaritons are hybrid light-matter quasi-particles formed by the strong coupling between excitons (electron-hole pairs) in semiconductor materials and photons in photonic structures, such as cavity or photonic crystal (PhC) slabs. In our project, we want to observe polaritonic bands using molybdenum diselenide ($MoSe_2$) monolayer and PhC slab.

Summary of Research:

To realize strong coupling, the coupling strength should be far greater than the linewidth of excitonic resonance and the linewidth of photonic resonance. Narrow linewidth of photonic resonance is easier to achieve compared to excitonic resonance. Therefore, a narrower linewidth of excitonic resonance is preferred in our experiment. The linewidth of excitons in $MoSe_2$ monolayer is easily affected by surrounding dielectric environment. People usually encapsulate the monolayer with hBN flakes, which have atomically flat surface to reduce the inhomogeneous broadening [1.] However, it's not doable for us now because the lateral size of PhC slabs is at least larger than 100 μm for observing a good band in experiment, and it is difficult to get very large and high quality hBN thin flakes by mechanical exfoliation. Also, large size $MoSe_2$ monolayers cannot be obtained by mechanical exfoliation. Good thing is that recently people can use gold exfoliation to get millimeter scale monolayers [2]. And dodecanal encapsulation method is used to make the gold exfoliated monolayer more intrinsic [3]. We are using these dodecanal encapsulated and gold exfoliated $MoSe_2$ monolayers in our devices.

The PhC slabs we used are square lattices in silicon nitride layer. The square lattice consisted of air cylinder holes that were fabricated by etching the silicon nitride layer and later filled by plasma enhanced chemical vapor deposition (PECVD) TEOS oxide left a unflatten surface. To avoid the influence to monolayer caused by unflatten surface of PhC slab, chemical mechanical polishing (CMP) is needed.

Conclusions and Future Steps:

We already used PECVD TEOS to fill the air cylinder holes very well without voids. However, CMP process needs some improvements to get flat surface. And we already made some devices (Figure 1) but haven't observe polaritonic bands due to the unsuccessful CMP process which left unflatten surface and influenced the linewidth of excitonic resonance.

We will continue to improve CMP process and hopefully we will get some good data soon.

References:

[1] F. Cadiz, et al., Excitonic Linewidth Approaching the Homogeneous Limit in MoS2-Based van der Waals Heterostructures. Phys. Rev. X 7, 021026 (2017).

[2] Li, Q., et al. Macroscopic transition metal dichalcogenides monolayers with uniformly high optical quality. Nat Commun 14, 1837 (2023).

[3] Liu, F., et al. Disassembling 2D van der Waals crystals into macroscopic monolayers and reassembling into artificial lattices. Science 367, 903-906 (2020).

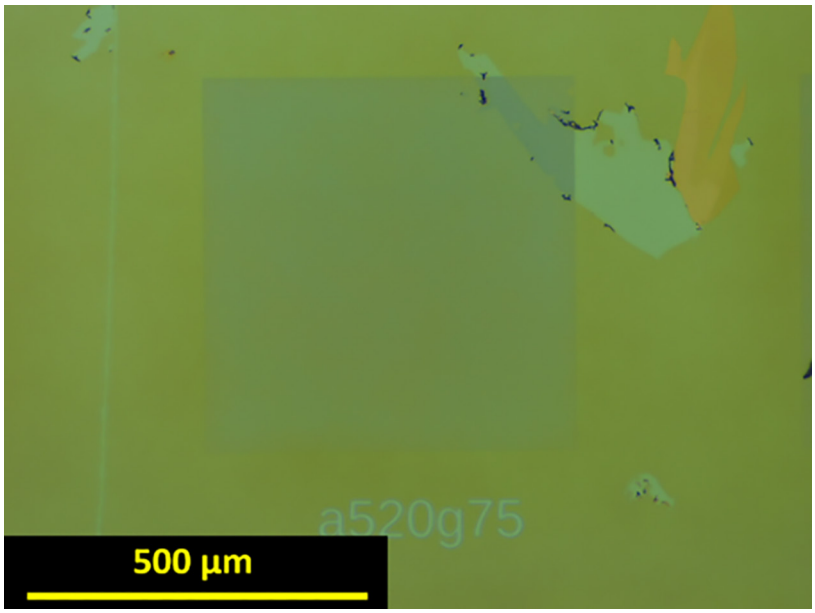

Figure 1: Dodecanal encapsulated $MoSe_2$ monolayer on a square lattice PhC slab.

Using Photolithography to Mass-Produce Rings of Controlled Size

CNF Project Number: 3123-23
Principal Investigator(s): Sarah Hormozi
User(s): Jonathan Lalieu

Affiliation(s): Smith School of Chemical and Biomolecular Engineering, Cornell University

Primary Source(s) of Research Funding: National Science Foundation

Contact: hormozi@cornell.edu, jkl227@cornell.edu
Research Group Website: https://hormozi.cbe.cornell.edu/

Primary CNF Tools Used: Heidelberg DWL2000, GCA AS200 i-line Stepper

Abstract:

The CNF user of the project trained on photolithography tools. We established that photolithography of SU-8 was an acceptable process to achieve our end goal of mass-producing rings of controlled size and aspect ratio, above ten micrometers, to use in rheology experiments of dense suspensions. We refined a recipe for the proper spinning, exposure and collection of said rings. We started the mass-production of one size of rings, that we have been able to use in rheology experiments. These experiments showed that, as we expected, the high aspect-ratio of these shapes induced a large additional stress in the rheology of the suspension, in the form of a rolling resistance in the contact between particles.

Summary of Research:

Our research focuses on the rheology of dense suspension, and more specifically on the role of rolling friction between particles. This rolling friction is purely geometrical [1], so we decided to focus on square cross-section ring-shaped particles because of their high symmetry. The rolling friction is then controlled by the aspect ratio between the thickness of the ring and its outer diameter. With rings, a large rolling friction coefficient can be achieved, which in turn will induce a large change in the jamming solid volume fraction for a contact-driven flow of a suspension [2,3].

We first prepared a photolithography mask with the Heidelberg DWL2000 mask writer that had rings of multiple sizes and aspect ratios to test the range of shape we could achieve. We spun SU-8 10 on 100 mm silicon wafers and refined the spinning speed to achieve a reproducible thickness of 20 μm, homogeneous on the wafer with a relative variation under 2%. We then exposed the wafers using the GCA AS200 i-line Stepper. We adjusted the exposure procedure to obtain polymerized devices of a good quality, both in adequation with their size on the mask and with large enough stiffness, as shown on Figure 1.

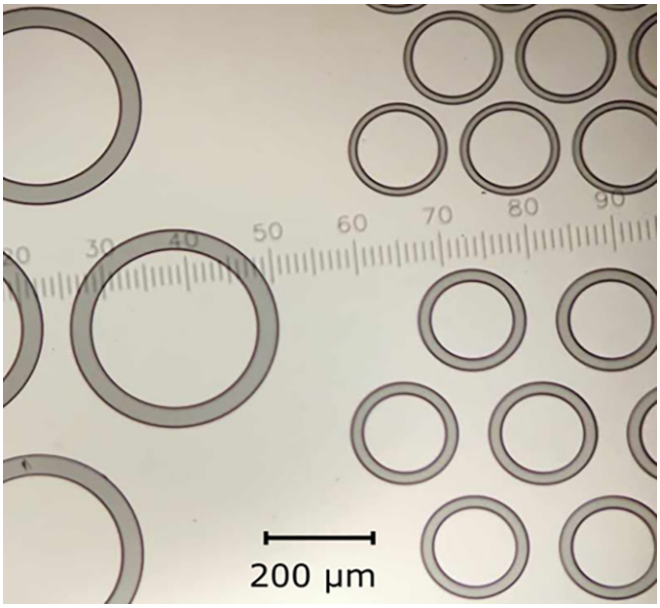

Figure 1: View of SU-8 rings on a wafer through a microscope, with two different diameters and aspect ratios.

We then moved on to one specific size of rings for the mass-producing: rings of an outer diameter of 200 μm and a thickness of 20 μm. This aspect ratio of 10 is directly proportional to the rolling friction coefficient and translates to a rolling friction coefficient of 5, much higher than the sliding friction coefficient. With this, we expect the rolling friction to be dominant in the rheology of dense suspensions with a large contribution from the contacts between particles. Our objective was to produce a few millions of these rings, and we managed to produce 50.000 per wafer. The main difficulty has been the ability to collect the rings and lift them off the wafers. We found that adding a layer of Omni-Coat before spinning SU-8, then hard baking the rings at 190°C after developing, and shaving the wafers with a sharp razor blade in a

water bath allowed us to collect most of them without undermining their structural integrity (Figure 2).

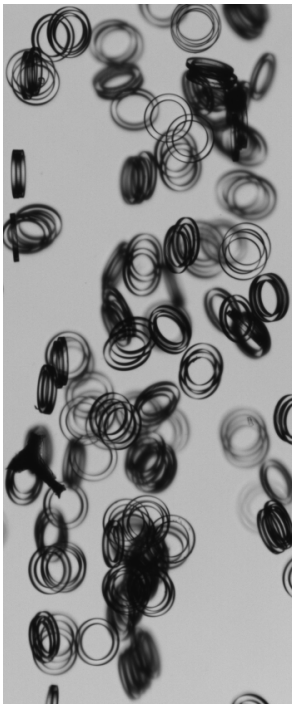

Figure 2: Photo captured of a flowing suspension made using SU-8 rings. The flow is in the downwards direction.

We just started doing rheology experiments using this batch of rings in a somewhat dense regime. The preliminary results show that for high shear-rates almost no contacts between particles are established, and we retrieve usual rheological behavior for suspension in the divergence of the viscosity with respect to the solid volume fraction. However, at low shear-rates the flow is mostly contact-driven, and we see the appearance of yield stresses at volume fraction much lower than what is usually seen for suspensions of spheres (Figure 3), as we expected when we settled on the ring-shape for the particles. Figure 2 also shows that the rings tend to align with each other, while having their main axis perpendicular to the flow direction.

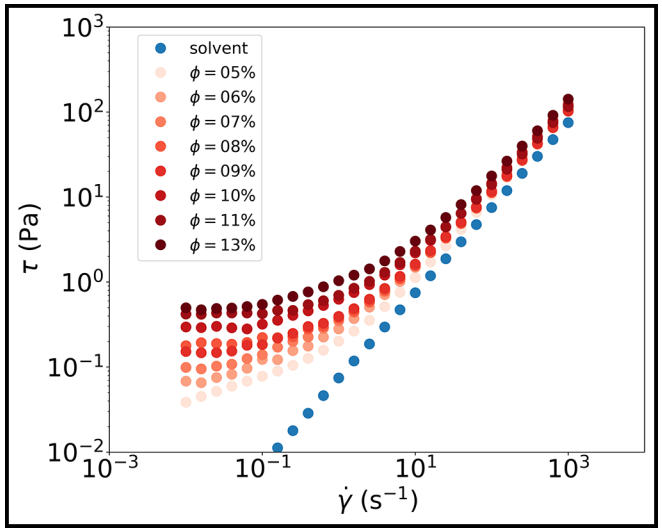

Figure 3: Shear stress as a function of shear-rate for different volume fraction, compared to the solvent alone.

References:

[1] Agarwal, et al. (2021). Rolling friction measurement of slightly non-spherical particles using direct experiments and image analysis. Granular Matter, 23(3), 60.

[2] Singh, et al. (2020). Shear thickening and jamming of dense suspensions: the "roll" of friction. Physical Review Letters, 124(24), 248005.

[3] d'Ambrosio, et al. (2023). The role of rolling resistance in the rheology of wizarding quidditch ball suspensions. Journal of Fluid Mechanics, 974, A36.